

Quantum Monte Carlo study of $S = 1/2$ weakly-anisotropic antiferromagnets on the square lattice

Alessandro Cuccoli,^{1,2} Tommaso Roscilde,^{3,4} Valerio Tognetti,^{1,2} Ruggero Vaia,^{5,2} and Paola Verrucchi^{1,2}

¹*Dipartimento di Fisica dell'Università di Firenze,*

via G. Sansone 1, I-50019 Sesto Fiorentino (FI), Italy

²*Istituto Nazionale per la Fisica della Materia (INFM),*

Unità di Ricerca di Firenze, via G. Sansone 1, I-50019 Sesto Fiorentino (FI), Italy

³*Dipartimento di Fisica 'A. Volta' dell'Università di Pavia, via A. Bassi 6, I-27100 Pavia, Italy*

⁴*Istituto Nazionale per la Fisica della Materia (INFM),*

Unità di Ricerca di Pavia, via A. Bassi 6, I-27100 Pavia, Italy

⁵*Istituto di Fisica Applicata 'Nello Carrara' del Consiglio Nazionale delle Ricerche, via Panciatichi 56/30, I-50127 Firenze, Italy*

(Dated: February 5, 2020)

We study the finite-temperature behaviour of two-dimensional $S = 1/2$ Heisenberg antiferromagnets with very weak easy-axis and easy-plane exchange anisotropies. By means of quantum Monte Carlo simulations, based on the continuous-time loop and worm algorithm, we obtain a rich set of data that allows us to draw conclusions about both the existence and the type of finite-temperature transition expected in the considered models. We observe that the essential features of the Ising universality class, as well as those of the Berezinskii-Kosterlitz-Thouless (BKT) one, are preserved even for anisotropies as small as 10^{-3} times the exchange integral; such outcome, being referred to the most quantum case $S = 1/2$, rules out the possibility for quantum fluctuations to destroy the long or quasi-long range order, whose onset is responsible for the Ising or BKT transition, no matter how small the anisotropy. Besides this general issue, we use our results to extract, out of the isotropic component, the features which are peculiar to weakly anisotropic models, with particular attention for the temperature region immediately above the transition. By this analysis we aim to give a handy tool for understanding the experimental data relative to those real compounds whose anisotropies are too weak for a qualitative description to accomplish the goal of singling out the genuinely two-dimensional critical behaviour.

PACS numbers: 75.10.Jm, 75.40.-s, 75.40.Mg, 75.40.Cx

I. INTRODUCTION

In the last few decades the Heisenberg antiferromagnet (HAFM) on the square lattice has been thoroughly studied by means of several theoretical, numerical and experimental techniques^{1,2,3}. Such research hands us a picture where three classes of substantially different models appear, the isotropic, the easy-axis, and the easy-plane antiferromagnets. The reference models for the two latter classes are the 2D-Ising and 2D-XY antiferromagnets, defining their respective universality class and known to display a finite-temperature phase transition. It is also known that quantum effects, despite being enhanced by the reduced dimensionality, do not substantially change the essential features of the above models, not even in the extreme $S = 1/2$ case, though evidently renormalizing their thermodynamic properties. This results from renormalization group^{4,5} and semiclassical approaches^{6,7}, as well as from quantum Monte Carlo (QMC) simulations^{8,9,10,11,12}.

In the above picture, however, there still is a grey area, where our knowledge is not detailed enough to allow a precise reading of the experimental data: this is the area of very weak anisotropies and strong quantum effects, which is of particular interest as most of the real layered compounds whose magnetic behaviour is properly modeled by the $S = 1/2$ HAFM on the square lattice

are characterized by anisotropies as small as 10^{-3} times the exchange integral. These compounds exhibit a phase transition at a finite temperature T_N which is often too large for the interlayer coupling to be the unique player, while the idea of a two-dimensional anisotropic criticality as the trigger of the transition appears well sound^{13,14}: such idea is corroborated by the measured values of some critical exponents¹⁵. The experimental observation tells us that three-dimensional long-range order is present below T_N and that well above T_N no trace of anisotropic behaviour is left; it is slightly above T_N that one hence expects evidences of genuine 2D anisotropic behaviour to be detectable. In order to let these experimental evidences surface out of the sea of the isotropic thermodynamics, precise numerical data for the $S = 1/2$ nearly isotropic HAFM are needed: it is the purpose of this work to fulfill such need. In particular, we address the problem of the existence and characterization of the phase transition, making use of continuous-time QMC cluster algorithms, which are well suited in the neighbourhood of a critical point, since they do not suffer from critical slowing-down. The general resulting picture is that a phase transition is induced by an arbitrary amount of anisotropy, and that several distinctive features of the expected universality class can be traced out.

The structure of the paper is as follows: in Section II the general properties of the anisotropic models are described, extracting the most significant difference with

respect to the isotropic model. In Section III the QMC methods are presented, the thermodynamic quantities under investigation are defined, and the finite-size scaling (FSS) theory used in our analysis is briefly recalled. The results for nearly isotropic models, as from both FSS analysis and thermodynamic behaviour, are presented and discussed in Sections IV and V for the easy-axis and easy-plane case, respectively. In Section VI the critical-temperature vs anisotropy phase-diagram is discussed. Eventually, conclusions are drawn in Section VII.

II. THE TWO-DIMENSIONAL XXZ MODEL ON THE SQUARE LATTICE

The XXZ model is defined by the Hamiltonian

$$\hat{\mathcal{H}} = \frac{J}{2} \sum_{\mathbf{i}, \mathbf{d}} \left[(1 - \Delta_\mu) (\hat{S}_{\mathbf{i}}^x \hat{S}_{\mathbf{i}+\mathbf{d}}^x + \hat{S}_{\mathbf{i}}^y \hat{S}_{\mathbf{i}+\mathbf{d}}^y) + (1 - \Delta_\lambda) \hat{S}_{\mathbf{i}}^z \hat{S}_{\mathbf{i}+\mathbf{d}}^z \right], \quad (1)$$

where $\mathbf{i} = (i_1, i_2)$ runs over the sites of an $L \times L$ square lattice, \mathbf{d} connects each site to its four nearest neighbours, $J > 0$ is the antiferromagnetic exchange integral, Δ_μ and Δ_λ are the easy-axis (EA) and easy-plane (EP) anisotropy parameters, respectively, hereafter getting positive values smaller than unity. As J sets the energy scale, the dimensionless temperature $t \equiv k_B T/J$ will be used in the following.

The spin operators $\hat{S}_{\mathbf{i}}^\alpha$ ($\alpha = x, y, z$) obey the $su(2)$ commutation relations $[\hat{S}_{\mathbf{i}}^\alpha, \hat{S}_{\mathbf{j}}^\beta] = i\epsilon^{\alpha\beta\gamma} \delta_{ij} \hat{S}_{\mathbf{i}}^\gamma$ and are such that $|\hat{\mathbf{S}}|^2 = S(S+1)$.

Besides the isotropic model $\Delta_\lambda = \Delta_\mu = 0$, Eq. (1) defines the EA ($\Delta_\lambda = 0$, $0 < \Delta_\mu \leq 1$) and EP ($\Delta_\mu = 0$, $0 < \Delta_\lambda \leq 1$) magnets, whose respective reference models are the Ising model ($\Delta_\mu = 1$) and the XY (also known as XX0) one ($\Delta_\lambda = 1$).

What is known about these models can be summarized as follows:

i) the isotropic model has no finite-temperature transition; its ground state is ordered for any S and a critical region of divergent correlations is clearly observed at very low temperatures;

ii) the EA models exhibit an Ising-like transition at a critical temperature t_{I} which is an increasing function of both Δ_μ and S ; for $S \geq 1$, t_{I} is finite for all anisotropies;

iii) the EP models exhibit a transition of the Berezinskii-Kosterlitz-Thouless (BKT) type, at a critical temperature t_{BKT} which is an increasing function of both Δ_μ and S ; for $S \geq 1$, t_{BKT} is finite for all anisotropies.

Some of the above statements are rigorously proved, others come from the combination of theoretical, numerical and experimental results.

More precisely, for what concerns ground state properties, an antiferromagnetically ordered ground state has been exactly proved^{16,17} for $S = 1/2$ only in the case of strong anisotropy, $\Delta_\lambda > 0.88$ and $\Delta_\mu > 0.32$. For weaker

anisotropies clear numerical evidence exists of an ordered ground state down to the isotropic limit, as coming from QMC and exact diagonalization studies¹⁸. As for the finite-temperature properties, according to renormalization group analysis^{5,19}, the critical temperature vanishes in the isotropic limit as $t_{\text{I}, \text{BKT}} \sim [\ln(\text{const.}/\Delta_{\mu, \lambda})]^{-1}$. In the EA case the existence of the transition for arbitrary Δ_μ has been rigorously proved only in the classical limit $S \rightarrow \infty$, while in the quantum case the proof is restricted to a spin-dependent finite amount of anisotropy²⁰. In the EP case the situation is even less clear, since also in the classical limit a rigorous proof²¹ of the existence of a transition is limited to the case $\Delta_\lambda \gtrsim 0.553$, while no rigorous proof exists in the quantum case.

In the $S = 1/2$ case, evidences of a phase transition for anisotropies as small as $\Delta_\mu = 0.01$ in the EA case^{8,9} and $\Delta_\lambda = 0.02$ in the EP case¹⁰ were suggested by previous QMC approaches; however, these computations employed local algorithms which cannot easily access the critical region and a rigorous FSS analysis could not be performed. The situation is still unclear also because recent works based on real-space renormalization-group^{22,23} predict the existence of a critical value of the anisotropy in the EA case ($\Delta_\mu^{(c)} \approx 0.2$) below which the transition would be destroyed by quantum fluctuations. In this work we hence consider $S = 1/2$ and four nearly isotropic systems, two EA, $\Delta_\mu = 0.01$ and $\Delta_\mu = 0.001$, and two EP ones, $\Delta_\lambda = 0.02$ and $\Delta_\lambda = 0.001$.

III. QUANTUM MONTE CARLO, OBSERVABLES AND FINITE-SIZE EFFECTS

A. Quantum Monte Carlo method: continuous-time algorithms

As usually done in the existing literature on QMC, in this section and in appendices A and B we employ the notation

$$J^{XY} \equiv J(1 - \Delta_\mu), \quad J^Z \equiv J(1 - \Delta_\lambda), \quad (2)$$

and $\beta \equiv 1/k_B T$.

The QMC method for the $S = 1/2$ XXZ model is based on the Trotter-Suzuki decomposition of the partition function, which can be approximated by the following expression²⁴:

$$\mathcal{Z}(\beta) \equiv \text{Tr } e^{-\beta \hat{\mathcal{H}}} \approx \sum_{\mathcal{S}} \prod_n w_{p_n, s}(\Delta\tau), \quad (3)$$

where w_p represents the amplitude of propagation of a pair of nearest-neighbour spins from a configuration $|\sigma_i, \sigma_j\rangle$ to $|\sigma'_i, \sigma'_j\rangle$ in the (imaginary-) time step $\Delta\tau = \beta/(zM)$, M being the Trotter number, z the coordination number and $|\{\sigma_i\}\rangle$ ($\sigma_i = \pm 1/2$) the basis set diagonalizing the \hat{S}_i^z operator. The two bond configurations define a space-time *plaquette* configuration $p = \{\sigma_i, \sigma_j; \sigma'_i, \sigma'_j\}$, so that w_p can be seen also as the weight of a given

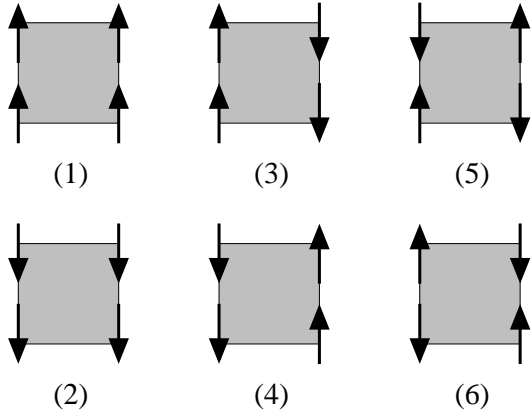


FIG. 1: Plaquette configurations with non-vanishing weights in the $S = 1/2$ XXZ model. The vertical axis is the imaginary-time direction.

plaquette configuration p . The index n runs over all plaquettes on the space-time lattice, and the index \mathcal{S} runs over all configurations of the system. At each time step plaquettes are defined on different groups of bonds $\langle ij \rangle$, so that all bonds involved in the propagation at the same time step do not share any spin; moreover, each plaquette shares its corner spins with two plaquettes on the previous and two on the subsequent time step. The expression (3) becomes exact in the limit $M \rightarrow \infty$.

In the case of the XXZ model, only the 6 plaquette configurations shown in Fig. 1 have non-zero weights w_p , whose expansion to first non trivial order in $\Delta\tau$ are^{25,26}:

$$\begin{aligned} w_1 = w_2 &\approx 1 - \frac{J^Z}{4} \Delta\tau \\ w_3 = w_4 &\approx 1 + \frac{J^Z}{4} \Delta\tau \\ w_5 = w_6 &\approx \frac{J^{XY}}{2} \Delta\tau. \end{aligned} \quad (4)$$

Plaquettes 1, 2, 3, and 4 propagate the state of the spin pair unchanged, while plaquettes 5 and 6 introduce an exchange of state for the interacting spins, hereafter denoted as *kink*.

Any standard Monte Carlo (MC) method can be applied for numerically evaluating the partition function (3); in principle one could do single local Metropolis moves which update clusters of plaquettes sharing corner spins in order to move to configurations with non-zero weight²⁷. This approach is however inconvenient, being affected by the well-known critical slowing-down. Moreover, in order to control the Trotter-approximation error, it is necessary to repeat the simulation for increasing Trotter number. In recent years efficient cluster algorithms were proposed to overcome the problem of critical slowing down in QMC simulations. In the context of quantum spin systems, the *loop-cluster algorithm* and the *worm algorithm* have revealed very effective; moreover, they can be also formulated in continuous

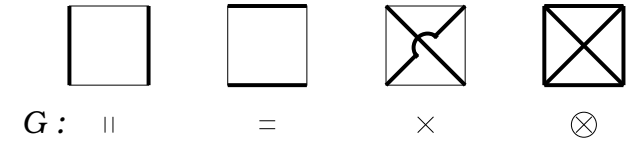


FIG. 2: Breakup decompositions of a single plaquette in the $S = 1/2$ XXZ model; thick lines join grouped spins.

imaginary time, thus removing completely the Trotter-approximation error.

1. Loop algorithm

One can completely eliminate the critical slowing-down by introducing the so-called *loop-cluster algorithm*²⁵, which is the quantum analog of the Swendsen-Wang²⁸ and Wolff²⁹ cluster algorithms introduced for classical spin systems. Within the multi-cluster approach¹² (analogue to the Swendsen-Wang scheme) the loop algorithm consists of probabilistically assigning to each plaquette a *break-up decomposition* (or graph) G , i.e., a way of grouping its spins in subgroups, so that the grouped spins can be flipped all at once bringing the plaquette into a configuration with non-vanishing weight; in the case of the XXZ model the above condition allows only grouping of spins into pairs (*non-freezing* breakups) or all together (*freezing* breakup), as shown in Fig. 2. Assigning a breakup G to each plaquette, one univocally defines a breakup decomposition $\mathcal{G} = \{G_n\}$ of the whole configuration $\mathcal{S} = \{\sigma_{i,\tau}\}$ into loops. Different breakup decompositions G are assigned to each plaquette configuration p according to weights $w(p, G)$ obeying the general sum rule $w_p = \sum_G w(p, G)$. Since the XXZ model is symmetric under time reversal, it is straightforward to require that plaquettes connected by time-reversal must have the same weights, i.e., $w(1, G) = w(2, G)$, $w(3, G) = w(4, G)$ and $w(5, G) = w(6, G)$. These weights must be positive and obey the detailed balance condition. The presence of frozen plaquettes leads to the generation of very big loops, whose flip is expected to be less and less effective in generating successive uncorrelated configurations; therefore, a general strategy to be followed is that of minimizing the probability of frozen plaquettes to appear. If one sets $w(p, \otimes) = 0$ for each p , a solution with positive breakup weights is obtained only in the case $J^{XY} \geq J^Z$, i.e., in the EP and isotropic case. When $J^Z > J^{XY}$, i.e., in the EA case, one must allow for freezing of at least a single plaquette configuration to achieve positivity. In particular, in the antiferromagnetic case, it is $w(3, \otimes) \equiv w(4, \otimes)$ that must be different from zero in order to have positive weights. By further imposing independence of the breakup decomposition from the plaquette configuration, i.e.,

$$\begin{aligned} w(1, ||) = w(3, ||) &\quad w(1, \times) = w(5, \times) \\ w(3, =) = w(5, =) &\quad , \end{aligned} \quad (5)$$

one gets that, within the same loop decomposition \mathcal{G} , all of the configurations \mathcal{S}' obtained from the starting one \mathcal{S} by flipping some of the loops, are reached with the same probability, i.e., each loop is flipped independently of all the other ones.

The complete set of non-zero breakup weights used in our calculation thus reads²⁵ (to first order in $\Delta\tau$):

- Easy-plane and isotropic case ($J_x \geq J_z$):

$$\begin{aligned} w(1, \parallel) &= 1 - \frac{J^{XY}}{4} \Delta\tau \\ w(1, \times) &= \frac{J^{XY} - J^Z}{4} \Delta\tau \\ w(3, =) &= \frac{J^{XY} + J^Z}{4} \Delta\tau; \end{aligned} \quad (6)$$

- Easy-axis case ($J_x < J_z$):

$$\begin{aligned} w(1, \parallel) &= 1 - \frac{J^Z}{4} \Delta\tau \\ w(3, =) &= \frac{J^{XY}}{2} \Delta\tau \\ w(3, \otimes) &= \frac{J^Z - J^{XY}}{2} \Delta\tau. \end{aligned} \quad (7)$$

The fact that freezing is required in the EA case can be physically interpreted as a reflection of the enforced antiferromagnetic correlations of the z -component of the spins: as a matter of fact, freezing of plaquettes of type 3 and 4 implies preservation of nearest-neighbour antiferromagnetic correlation along the MC flow, i.e., antiferromagnetic configurations are more “resistant” to MC fluctuations, with respect to ferromagnetic ones.

In the limit of continuous imaginary time³⁰, $\Delta\tau \rightarrow 0$, plaquettes with no *kink*, i.e., of types 1 (2) and 3 (4), acquire unitary weight, while plaquettes with a *kink*, i.e., of type 5 (6), get an infinitesimal weight, still keeping a finite weight per unit time $\omega_p = \lim_{\Delta\tau \rightarrow 0} w_p / \Delta\tau$; therefore kink-bearing plaquettes must be regarded as Poissonian events in the imaginary-time evolution of each pair of interacting spins. At the same time the breakup decomposition creating no *kink* in imaginary time evolution, acquires a unitary weight, while all the other breakups acquire infinitesimal weight, still keeping a finite weight per unit time $\omega(p, G)$. In the case of plaquette 5 (6), since the breakup weights have to be normalized to the plaquette weights, they become finite probabilities

$$p(5, =) = \frac{1}{2} \left(1 + \frac{J^Z}{J^{XY}} \right) \quad p(5, \times) = 1 - p(5, =) \quad (8)$$

in the EP case, and $p(5, =) = 1$, $p(5, \times) = 0$ in the EA case.

The algorithm then proceeds as follows:

- distribute breakups \times , $=$ and \otimes on the continuous segments (= infinite sequences of infinitesimal

plaquettes 1(2) and 3(4)) along the imaginary-time evolution of each pair of interacting spins, according to the Poisson distribution having as parameter $\beta \omega(p, G)$; for each kink in the propagation, choose a breakup with probabilities $p(5, G)$.

- reconstruct the loops defined by the decomposition of each infinitesimal plaquette;
- decide whether to flip each loop independently with probability one half.

The above procedure (multi-cluster update) represents a single MC step in our code. We have generally performed 10^4 MC steps for thermalization for each value of the temperature, and $1 \div 1.5 \cdot 10^5$ MC steps for evaluation of thermodynamic observables. The algorithm is very efficient in both the EA and the EP case, with autocorrelation times which always remain around unity for all the lattice sizes L we considered, i.e., $L = 16, 32, 64, 128, 200$. The autocorrelation time τ_c has been estimated by the blocking technique as:

$$\tau_c = \frac{n_b}{2} \frac{\sigma_x^2}{\sigma_x^2} \quad (9)$$

where σ_x^2 is the variance of the time-series $\{x_i\}$ ($i = 1, \dots, N_{\text{steps}} = n_b N_b$) produced for the variable x , while σ_X^2 is the variance of the block variable $X_j = N_b^{-1} \sum_{i=(j-1)*N_b+1}^{j*N_b} x_i$ ($j = 1, \dots, n_b$), with $N_b \gg \tau$ for the estimate to be sensible.

The introduction of freezing breakups has the effect of making a loop branch into subloops; as the flip of large branched clusters is less effective in generating successive uncorrelated configurations, the inclusion of freezing is generally thought to lower the efficiency of the loop algorithm²⁵, although no direct evidence of such conclusion exists. Nevertheless, for the EA anisotropies we consider, no significant loss of efficiency (i.e., increase in correlation time) is observed. Moreover, in the Ising limit, the above algorithm reproduces the Swendsen-Wang algorithm for the Ising model, which is known not to suffer from slowing down; therefore efficiency is possibly lost only for intermediate values of the anisotropy, which is not the case we are interested in.

We have implemented improved estimators^{29,31} for all the quantities of interest. A separate, more careful analysis is needed in the case of off-diagonal observables, whose most general bilinear example may be $\langle \hat{S}_i^+(\tau) \hat{S}_j^-(\tau') \rangle$. In absence of freezing, the improved estimator simply reads^{31,32}: $(\hat{S}_i^+(\tau) \hat{S}_j^-(\tau'))_{\text{impr}} = 1$, if (i, τ) and (j, τ') belong to the same loop, $= 0$ otherwise. This result can be understood by observing that the quantity we are considering may be seen as the ratio between the partition function of the system with density operator $\hat{S}_i^+(\tau) \hat{S}_j^-(\tau') \exp(-\beta \hat{H})$ and the partition function of the original model considered, with density operator $\exp(-\beta \hat{H})$. The final outcome for the estimator given above thus follows from the observation that in absence

of freezing, i.e., in the isotropic or EP class, according to Eqs. (6) the weight assigned to a loop decomposition is actually independent of the configuration onto which it is defined, since each kind of breakup has the same weight on every plaquette configuration where its weight is non-zero; therefore the same loop decomposition is reached with equal probability in the original and in the modified system, with the additional constraint, in the case of the modified system, that the two points (i, τ) and (j, τ') must belong to the same loop.

When freezing is present, the above argument breaks down, since only one plaquette configuration admits freezing and the constraint of having (i, τ) and (j, τ') on the same loop is no longer sufficient to have a non-zero contribution to the estimator. In principle it is possible to define the estimator for off-diagonal observables even in case of freezing; however, not only its implementation is highly non trivial from the point of view of programming, but its evaluation would also consume a considerable amount of computational time. As a matter of fact, for each pair of points (i, τ) , (j, τ') belonging to the same branch of a loop, one should look for freezing breakups by checking all the loop segments between the two points, an operation that, being the loops structure involved, becomes very costly at low temperatures. We have therefore renounced to implement such estimators in case of freezing. To have a complete picture of the thermodynamics of the system in the EA case we have then resorted to a different (and generally less efficient) QMC scheme, within which the calculation of the off-diagonal observables in the EA case is relatively straightforward, i.e., to the so-called worm algorithm.

2. Worm algorithm

The *worm* algorithm represents an alternative way to overcome the problem of critical slowing down in QMC simulations. The original idea of the algorithm can be found in Ref. 33, but we here formulate the algorithm in a different way, so that it appears as a direct generalization of the loop algorithm; our formulation is more directly related with the so-called "operator-loop update" introduced in the framework of the stochastic series expansion³⁴.

The worm algorithm starts by choosing a point at random in space-time, inserting two discontinuities in the local imaginary-time evolution, and then keeping one fixed (the "tail" of the worm) while letting the other (the "head" of the worm) freely travel through the lattice. The single-worm update ends when the head happens to "eat" the tail (the worm closes), so that the isolated discontinuities disappear and the system is led to a new configuration having non-zero weight. All the segments of imaginary-time evolution touched by the worm's head have to be flipped, i.e., the worm's head performs a real-time update of the system. Its motion conventionally goes forward (backward) in imaginary time while updat-

ing segments with up (down) spins, and it is ruled by detailed balance condition, to be locally satisfied on each (infinitesimal) plaquette it touches. In the context of the worm algorithm one has to abandon the concept of plaquette breakup, and the decision about how a plaquette is passed through by the worm must be taken from time to time. One of the distinctive feature of the algorithm is that the worm can pass through the same plaquette many times, each time in a different way, depending on the local configuration left at its previous passage.

General detailed balance conditions for the single plaquette update when the worm's head passes through it, flipping two spins, read

$$\begin{aligned} w_1 p(1 \rightarrow 3) &= w_3 p(3 \rightarrow 1) \\ w_1 p(1 \rightarrow 5) &= w_5 p(5 \rightarrow 1) \\ w_3 p(3 \rightarrow 5) &= w_5 p(5 \rightarrow 3), \end{aligned} \quad (10)$$

where we have already introduced the time- and space-reversal symmetries, so that here "1" means 1 or 2, "3" means 3 or 4, and "5" means 5 or 6, depending on the way the worm's head travels through the plaquette. Moreover, the transition probabilities must satisfy the sum rules

$$\begin{aligned} p(1 \rightarrow 3) + p(1 \rightarrow 5) &= 1 \\ p(3 \rightarrow 1) + p(3 \rightarrow 5) &= 1 \\ p(5 \rightarrow 1) + p(5 \rightarrow 3) &= 1. \end{aligned} \quad (11)$$

Moving to the continuous-time limit, we express the transition probabilities from a plaquette with a non-vanishing weight to another plaquette, as

$$\begin{aligned} p(1 \rightarrow 3) &= 1 + \pi(1 \rightarrow 3) \Delta\tau \\ p(3 \rightarrow 1) &= 1 + \pi(3 \rightarrow 1) \Delta\tau \\ p(1 \rightarrow 5) &= \pi(1 \rightarrow 5) \Delta\tau \\ p(3 \rightarrow 5) &= \pi(3 \rightarrow 5) \Delta\tau, \end{aligned} \quad (12)$$

where $\pi(1 \rightarrow 5)$ and $\pi(3 \rightarrow 5)$ have the meaning of (positive) transition probabilities per unit imaginary time, while $\pi(1 \rightarrow 3)$ and $\pi(3 \rightarrow 1)$ are (negative) corrections to the transition probabilities among plaquettes taking non-vanishing weights; these corrections arise from the poissonian occurrence of kinks in imaginary-time evolution. With the above parameterization of the transition probabilities, the first two of the sum rules (11) take the form

$$\begin{aligned} \pi(1 \rightarrow 3) + \pi(1 \rightarrow 5) &= 0 \\ \pi(3 \rightarrow 1) + \pi(3 \rightarrow 5) &= 0, \end{aligned} \quad (13)$$

while the third remains unchanged, as $p(5 \rightarrow 1)$ and $p(5 \rightarrow 3)$ keep their meaning of dimensionless probabilities for the different ways the worm's head can pass through a kink in imaginary-time evolution. The set of detailed balance equations in the continuous-time limit takes the

form

$$\begin{aligned}\pi(1 \rightarrow 3) - \pi(3 \rightarrow 1) &= \frac{J^Z}{2} \\ \pi(1 \rightarrow 5) &= \frac{J^{XY}}{2} p(5 \rightarrow 1) \\ \pi(3 \rightarrow 5) &= \frac{J^{XY}}{2} p(5 \rightarrow 3) .\end{aligned}\quad (14)$$

Together with the sum rules, they give as unique solution the following set of transition probabilities:

$$\begin{aligned}\pi(1 \rightarrow 5) &= \frac{J^{XY} - J^Z}{4} \\ \pi(3 \rightarrow 5) &= \frac{J^{XY} + J^Z}{4} \\ p(5 \rightarrow 3) &= \frac{1}{2} \left(1 - \frac{J^Z}{J^{XY}}\right) .\end{aligned}\quad (15)$$

It is immediate to see that this solution is equivalent to the set of breakup weights (6), which means that, at this level, the worm algorithm is nothing but the Wolff-type (single-cluster) version of the loop algorithm. However, as seen in the loop algorithm, in the EA case transition probabilities are not always positive, and some other transition mechanism must be invoked to overcome this problem. As seen before, the remedy in the case of the loop algorithm was to allow for branching of the loops; if one hence allows for branching also in the worm algorithm, the single-cluster version of the loop algorithm for the EA case is obtained.

A different strategy can be adopted in the case of the worm algorithm by introducing a new type of motion, named *bouncing*, where the worm's head, when attempting to update a plaquette, is bounced off and hence forced to locally trace back its route. From the physical point of view, the existence of a bounce mechanism protects some plaquettes from being updated, possibly those plaquettes containing local spin configurations which give a relevant contribution to the thermodynamics of the system; such local configurations are preserved along the MC flow and the effect of bouncing is seen to be very similar to that of freezing in the context of the loop algorithm. In the case of the EA antiferromagnet, the most relevant local configurations are those containing antiferromagnetic correlations of the z -components, i.e., in terms of plaquettes, $p=3,4$. Therefore, we allow for bounce on these plaquette configurations, introducing a finite bounce probability $p(3,b) = \pi(3,b)\Delta\tau$ which has to be accounted for in the sum rule

$$\pi(3 \rightarrow 1) + \pi(3 \rightarrow 5) + \pi(3,b) = 0 .\quad (16)$$

The detailed balance condition for the bounce probability is trivial, reading $p(3,b) w(3) = p(3,b) w(3)$. Eqs. (15) and (16) form an underdimensioned set and $\pi(3,b)$ can be hence chosen arbitrarily, with the only constraint of positive transition probabilities. As in the case of freezing,

it is highly convenient to minimize the bounce probability: when the worm's head bounces, part of its update operations are lost as it locally traces back its way, so that the efficiency in updating the configuration, keeping the number of elementary update operations fixed, is lowered. The following solution for the transition probabilities, minimizing the bounce probability, is found

$$\begin{aligned}\pi(1 \rightarrow 5) &= 0 \\ \pi(3 \rightarrow 5) &= \frac{1}{2} J^{XY} \\ \pi(3,b) &= \frac{1}{2} (J^Z - J^{XY}) \\ p(5 \rightarrow 1) &= 1 .\end{aligned}\quad (17)$$

The worm algorithm with the bounce process is a *pure-quantum* cluster algorithm: in the Ising model, which is a substantially classical statistical model, the algorithm loses its cluster nature, since only bounce processes survive, thus confining the worm on a single site. In this case the worm algorithm reproduces the single-flip Metropolis algorithm, as shown in Appendix A.

As in the case of the loop algorithm, each of our simulations consists of 10^4 MC steps for thermalization and of $1 \div 1.5 * 10^5$ MC steps for evaluation of thermodynamic observables. During thermalization, the number of worms to be produced at each step is adjusted so that the total length of the worms in the imaginary-time direction roughly equals the size of the $(D+1)$ -dimensional lattice, $L^2 * \beta$; this number is then kept fixed during the measurement phase. In this way, autocorrelation times of the order of unity are achieved for all values of the EA anisotropy considered. At variance with the loop algorithm, the efficiency is here expected to drastically decrease as the anisotropy increases, given that, as the model moves toward the Ising limit, the cluster algorithm transforms into the local Metropolis algorithm; however, the case of strong anisotropy is not of our interest here.

As mentioned in the previous section, the estimator for bilinear off-diagonal quantities like $\hat{S}_i^+(\tau)\hat{S}_j^-(\tau')$ can be thought of as a partition function for a modified model, in which two spin discontinuities are inserted in the system configuration at the points (i,τ) , (j,τ') . Now it becomes clear that configurations giving a non-zero contribution to such a partition function are generated during the worm update whenever the discontinuities associated to the head and tail of the worm coincide with the above points, both in the EA and in the EP case. Therefore the off-diagonal observables are measured on-the-fly during the motion of worm's head³³, and each worm update produces a statistics for the estimators which grows linearly with the length of the worm. As in the case of the loop algorithm, this kind of estimators give to the worm geometry a physical meaning: the further the worm head travels away from its tail, the larger will be the off-diagonal correlations. On the other hand, improved estimators are not defined for diagonal quantities in the EA case; to this respect, worm and loop algorithms are seen to be exactly complementary.

As final remark, we mention that the worm algorithm retains its full efficiency also in presence of a uniform magnetic field applied to the spins, while the loop algorithm is known to exponentially slow down as the field is increased and/or the temperature is lowered³⁵. Details of the worm algorithm in a finite field are not relevant to the present work and will be given in a forthcoming paper.

B. Thermodynamic quantities

We briefly report here the definition of the relevant thermodynamic quantities measured in our QMC study, together with their respective estimators. The MC average of the estimator will be hereafter denoted as $\langle \dots \rangle_{\text{MC}}$.

The internal energy $\langle \hat{\mathcal{H}} \rangle$ is estimated as the MC average of

$$\frac{1}{2\beta} \sum_{i,d} \int_0^\beta d\tau \phi_{i,d}(\tau) \equiv E, \quad (18)$$

where $\phi_{i,d}(\tau)$ takes the value $-J^Z/4$ if at imaginary time τ there is an infinitesimal plaquette configuration of type 1 (2), $J^Z/4$ if of type 3 (4), $-\delta(\tau)$ if of type 5 or (6). This corresponds to the continuous-time limit of the energy estimator as defined in Ref. 27.

The specific heat $c \equiv \beta^2(\langle \hat{\mathcal{H}}^2 \rangle - \langle \hat{\mathcal{H}} \rangle^2)/L^2$ is estimated from energy fluctuations as

$$\frac{1}{L^2} \left(\langle \beta^2 E^2 - N_{\text{kinks}} \rangle_{\text{MC}} - \beta^2 \langle E \rangle_{\text{MC}}^2 \right), \quad (19)$$

where N_{kinks} is the number of kinks present in each generated configuration. The variance of the specific heat has been estimated via binning analysis of the time series related to the energy estimator and the kink number.

The staggered magnetization $M_s \equiv (-1)^i \langle \hat{S}_i^z \rangle$ is estimated as the MC average of

$$\frac{1}{L^2} \sum_i (-1)^i \sigma_i^z \equiv m_s. \quad (20)$$

The spin-spin correlation function is

$$C^{\alpha\alpha}(\mathbf{r}) = \frac{1}{\beta^2} \int_0^\beta d\tau d\tau' \langle \hat{S}_i^\alpha(\tau) \hat{S}_{i+r}^\alpha(\tau') \rangle f(\tau, \tau'), \quad (21)$$

where $f(\tau, \tau') = \beta \delta(\tau - \tau')$ in the equal-time correlator (ET) and $f(\tau, \tau') = 1$ in the time-averaged (TA) one. In both cases the numerical calculation of the correlation function takes advantage of the existence of the improved estimator defined in the previous subsection.

The generalized susceptibility is

$$\chi^{\alpha\alpha}(\mathbf{q}) = \frac{\beta}{L^2} \sum_r e^{i\mathbf{q}\cdot\mathbf{r}} C^{\alpha\alpha}(\mathbf{r}); \quad (22)$$

the time-averaged susceptibility corresponds to the thermodynamic definition (second derivative of the free energy) while the equal-time one corresponds to $\beta * S(\mathbf{q})$,

where $S(\mathbf{q})$ is the static structure factor as measured, e.g., in neutron scattering experiments. From the general definition above follow those of the uniform susceptibility

$$\chi_u^{\alpha\alpha} = \chi^{\alpha\alpha}(\mathbf{q}=0), \quad (23)$$

and of the staggered one

$$\chi_s^{\alpha\alpha} = \chi^{\alpha\alpha}(\mathbf{q}=(\pi, \pi)). \quad (24)$$

Susceptibilities and correlation functions have been measured both along the z -axis (C^{zz} , χ^{zz}) and in the xy -plane ($C^{xx} = C^{yy}$, $\chi^{xx} = \chi^{yy}$); in the EA case, the latter have been evaluated by means of the worm algorithm. In what follows, we will show and comment our data relative to the uniform TA susceptibility and to the staggered ET susceptibility, being such quantities the more relevant ones from the experimental point of view.

The correlation length $\xi^{\alpha\alpha}$ is defined *via* the long-distance exponential decay of the staggered correlation function, $(-1)^r C^{\alpha\alpha}(\mathbf{r}) \sim \exp(-r/\xi^{\alpha\alpha})$ ($r \rightarrow \infty$). A direct estimate $\xi_{\text{fit}}^{\alpha\alpha}$ of the correlation length may be hence found by fitting the long-distance behaviour of $C^{\alpha\alpha}(\mathbf{r})$ with a model-dependent function, as discussed in the following sections. Such procedure, however, is strongly dependent on the quality and stability of the fit, and does not always lead to a univocally defined result in case of a finite-size system in presence of a phase transition, i.e., of a diverging correlation length. An alternative strategy, which we have also used, is offered by the so-called second moment definition³⁶

$$\xi_2^{\alpha\alpha} = \frac{L}{2\pi} \sqrt{\frac{\chi^{\alpha\alpha}(\pi, \pi)}{\chi^{\alpha\alpha}(\pi + 2\pi/L, \pi)} - 1}, \quad (25)$$

which can be directly extracted by the simulation data, supplemented by a binning analysis of susceptibility time series in order to estimate the variance.

Another relevant observable, in the EP case, is the helicity modulus Υ , which is a measure of the response of the system to the application of a twist Φ in the boundary condition along a given direction:

$$\Upsilon \equiv \frac{1}{J^{XY} L^2} \left[\frac{\partial^2 F(\phi)}{\partial \phi^2} \right]_{\phi=0}, \quad (26)$$

where $\phi = \Phi/L$. In Appendix B we show that, starting from the above definition as explicitly written in terms of spin operators, the estimator of the helicity modulus of the $S = 1/2$ XXZ EP model reads

$$\Upsilon = \frac{t}{2} |\mathbf{W}|^2, \quad (27)$$

where $\mathbf{W} = (W_1, W_2)$, $W_{1(2)}$ being the total winding number of spin paths (paths traced by a fixed spin configuration, up or down) in the 1(2) lattice direction. Remarkably, this estimator is directly related with that of the superfluid density of bosonic systems³⁷. An efficient improved version of the estimator (27) has been introduced by Harada and Kawashima¹² in the context of the loop algorithm, and is the one employed in this work.

C. Finite-size scaling

A FSS analysis³⁸ can give strong indications on the existence of a phase transition at some temperature t_c , possibly leading to a full characterization of its universality class. The simplest evidence that a transition occurs is found when, for increasing lattice size, the order parameter scales to a finite value below a certain temperature, indicating that a non-zero order parameter develops in the thermodynamic limit.

In the case of second-order phase transitions, the Ansatz³⁸ for the scaling behaviour of a generic finite-size thermodynamic quantity $A_L(t)$ in the neighbourhood of the critical point reads

$$A_L(t) \sim L^{\rho/\nu} F_A[L^{1/\nu}(t - t_c)], \quad (28)$$

where ρ is the critical exponent of $A \equiv A_\infty$, i.e., $A(t \rightarrow t_c) \sim |t - t_c|^{-\rho}$, ν is the exponent for the correlation length, while F_A is the universal scaling function. At the critical point Eq. (28) implies $A_L(t_c) \sim L^{\rho/\nu}$. In the case of ξ this means linear scaling at criticality, without any assumption on the universality class; therefore, looking for the temperature at which a properly defined³⁹ $\xi_L(t)$ scales linearly with the system size gives an unbiased estimate of the critical temperature. Eq. (28) implies that the scaling plot of $A_L L^{-\rho/\nu}$ vs $y = (t - t_c)L^{1/\nu}$, with a proper estimate of t_c , shows the data for different lattice sizes to collapse onto the universal curve $F_A(y)$.

In the case of a BKT transition, in which no order parameter is given, the presence of topological order at finite temperature is shown when the helicity modulus scales to a finite value below a certain temperature. The use of the scaling Ansatz to locate the critical temperature can be generalized to the case of a BKT transition, though most of the critical exponents are not defined. However the Kosterlitz-Thouless theory predicts $\eta = 1/4$ at the critical point, so that a scaling behaviour of the susceptibility as $L^{2-\eta} = L^{7/4}$ is a good signature of the critical temperature. Moreover, Kosterlitz's renormalization group equations⁴⁰ provide the critical scaling law for the helicity modulus in the form⁴¹

$$\frac{\Upsilon_L(t_{\text{BKT}})}{t_{\text{BKT}}} \approx \frac{2}{\pi} \left(1 + \frac{1}{2 \log(L/L_0)} \right), \quad (29)$$

where L_0 is a constant. This relation has been widely used to locate the BKT critical temperature of the classical 2D planar-rotator model^{42,43} and of the $S = 1/2$ quantum XY model¹².

We end this section with a general remark. It is observed that the smaller the anisotropy, the bigger the lattice sizes required to enter the asymptotic scaling regime, where FSS holds. This is essentially due to the fact that the critical region is shifted to lower temperature: the correlation length of the isotropic model, acting as a lower bound for that of the nearly isotropic ones, increases exponentially upon lowering the temperature,

and therefore, keeping the lattice size fixed, the ratio L/ξ_L , that drives the onset of asymptotic scaling near the transition, gets smaller.

IV. EASY-AXIS MODEL AND ISING TRANSITION

The values of the anisotropy here considered are $\Delta_\mu = 0.01$ (also used in Ref. 9) and $\Delta_\mu = 0.001$. They are comparable with the characteristic anisotropies of real compounds; yet, for such small anisotropy there is no universal consensus on the existence of a transition^{22,23}. From previous works^{7,8,9} the transition is expected in the temperature range $0.2 < t < 0.3$ in both systems. At higher temperature the behaviour gets closer to that of the isotropic model, which has been extensively investigated by means of QMC in recent years^{30,44,45,46}; we have extended our analysis up to $t \simeq 0.8$ in order to identify those deviations from the isotropic behaviour that can be experimentally detected above the critical region.

In our approach, evidences for the existence of an Ising-like transition follow from a detailed FSS analysis of the data; subsequently, we analyze the temperature dependence of some relevant thermodynamic quantities, emphasizing the signatures of the EA nature.

A. Finite-size scaling analysis

Our analysis proceeds in three steps: we give evidence for a transition to occur, then the transition temperature is located, and eventually the Ising critical scaling is tested. After the discussion made in Section III C the FSS analysis for $\Delta_\mu = 0.001$ is expected to be more delicate than for $\Delta_\mu = 0.01$. Indeed, for the lattice sizes used ($L \leq 128$) some quantities show to have well entered the asymptotic scaling regime, while others do not. Anyway, clear (though not complete) evidence for the Ising universality class is given also for $\Delta_\mu = 0.001$; larger lattices would be required to reach a full characterization.

Let us first consider the order parameter, i.e., the staggered magnetization given in Eq. (20). In Fig. 3 M_s for $\Delta_\mu = 0.001$ is seen to scale to a finite value if $t \lesssim 0.22$, so that the magnetization in the thermodynamic limit becomes finite; the same behaviour is *a fortiori* observed in the case $\Delta_\mu = 0.01$. We then invoke the scaling Ansatz (28) for the longitudinal correlation length ξ^{zz} . The scaling plot of ξ_{fit}^{zz} , as specifically defined in Section IV E below, is shown in Fig. 4 for $\Delta_\mu = 0.001$ and gives $t_1(\Delta_\mu=0.001) = 0.2225(15)$. A similar analysis yields $t_1(\Delta_\mu=0.01) = 0.2815(25)$.

Hitherto, no assumptions were made about the universality class. In order to identify it, we consider the so called Binder's fourth cumulant⁴⁷, shown in Fig. 5 and

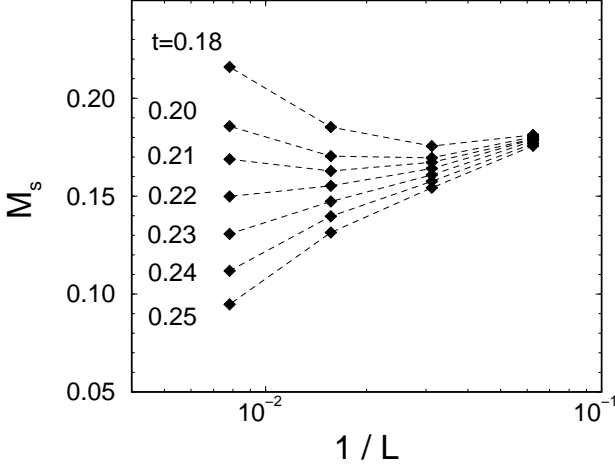


FIG. 3: Scaling of the staggered magnetization M_s in the EA model with $\Delta_\mu = 0.001$, for different t .

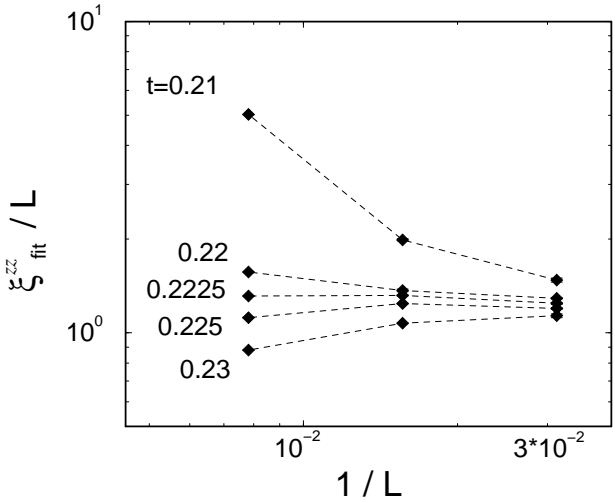


FIG. 4: Scaling of the longitudinal correlation length ξ_{fit}^{zz} in the EA model with $\Delta_\mu = 0.001$, for different t .

defined by

$$U_4 = 1 - \frac{\langle m_s^4 \rangle_{\text{MC}}}{3 \langle m_s^2 \rangle_{\text{MC}}^2}, \quad (30)$$

which assumes the universal critical value $U_4^{(c)} = 0.6106900(1)$ at t_1 in the 2D Ising model on the square lattice⁴⁸, and increases (decreases) with L , below (above) t_1 . For $\Delta_\mu = 0.01$, we verify such behaviour and obtain $t_1(\Delta_\mu=0.01) = 0.280(3)$, consistently with the above unbiased estimate from the scaling of ξ^{zz} . The scaling Ansatz (28) for the staggered magnetization, $M_s \sim L^{-\beta/\nu}$ at $t = t_1$, constitutes a further way of checking the 2D Ising behaviour, since the critical exponents $\beta = 1/8$ and $\nu = 1$ are involved. The data reported in Fig. 6 give $t_1 = 0.282(2)$. In the case of the weakest anisotropy $\Delta_\mu = 0.001$, both the Binder's fourth cumulant and the staggered magnetization have not yet well entered the

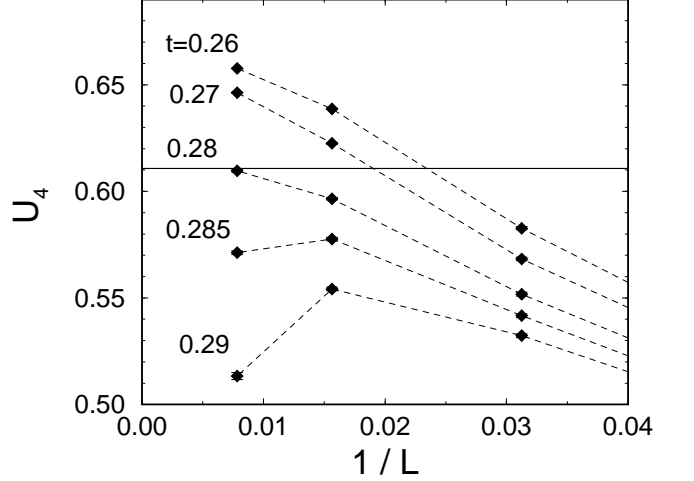


FIG. 5: Scaling of the Binder's fourth cumulant in the EA model with $\Delta_\mu = 0.01$ for different t . The solid line indicates the universal critical value $U_4^{(c)}$ (see text).

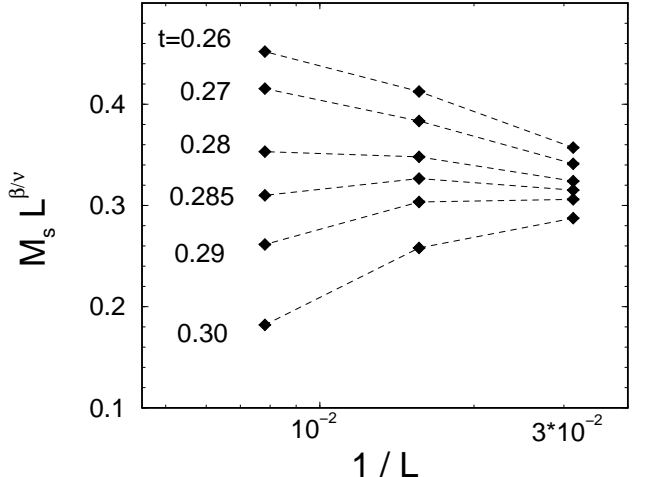


FIG. 6: Scaling of the staggered magnetization M_s in the EA model with $\Delta_\mu = 0.01$, for different t . The critical exponents $\beta = 1/8$ and $\nu = 1$ are those of the Ising universality class.

asymptotic scaling region for the lattice sizes considered, and t_1 cannot be reliably estimated by this technique.

A further test of the universality class involves the longitudinal staggered susceptibility χ_s^{zz} , Eq. (24): in this case the scaling Ansatz (28) gives $\chi_s^{zz}(t_1) \sim L^{\gamma/\nu}$, with 2D-Ising critical exponents $\gamma = 7/4$ and $\nu = 1$, as shown in Fig. 7 for the case $\Delta_\mu=0.001$. The estimated critical temperatures result $t_1(\Delta_\mu=0.01) = 0.2825(25)$ and $t_1(\Delta_\mu=0.001) = 0.2235(15)$, in full agreement with the above unbiased estimates.

To summarize, in the case $\Delta_\mu = 0.01$ we find consistency for the 2D-Ising critical exponent ratios β/ν and γ/ν , thus fully verifying the universality class. For $\Delta_\mu = 0.001$ the evidence, though limited to the matching of the estimates of t_1 obtained in Figs. 4 and 7, is quite

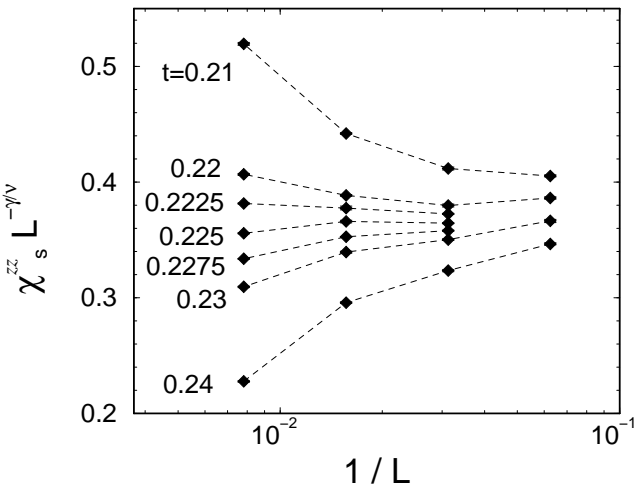


FIG. 7: Scaling of the longitudinal staggered susceptibility χ_s^{zz} in the EA model with $\Delta_\mu = 0.001$, for different t . The critical exponents $\gamma = 7/4$ and $\nu = 1$ are those of the Ising universality class.

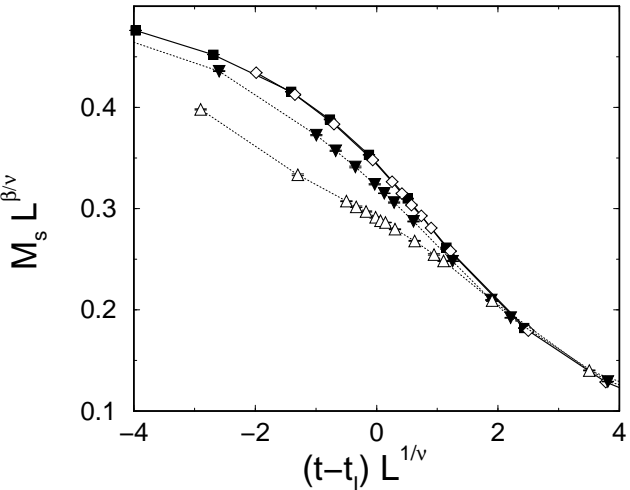


FIG. 8: Scaling plot for the staggered magnetization M_s in the EA model with $\Delta_\mu = 0.01$, for $L = 16$ (up triangles), 32 (down triangles), 64 (diamonds), 128 (squares). The critical exponents $\beta = 1/8$ and $\nu = 1$ are those of the Ising universality class, and the critical temperature is taken as $t_1 = 0.281$.

convincing.

As a check that the magnetization and the staggered susceptibility have actually reached the asymptotic scaling regime with the considered lattice sizes, we have constructed their scaling plots after Eq. (28), which are reported in Figs. 8 and 9. Data collapse for different lattice sizes is verified for the staggered susceptibility in the case $\Delta_\mu = 0.001$ for $L \geq 64$, taking $t_1 = 0.223$, and *a fortiori* in the case $\Delta_\mu = 0.01$; the staggered magnetization is instead seen to have entered the asymptotic scaling regime for $L \geq 64$ only in the case $\Delta_\mu = 0.01$.

From the above analysis a strong indication for the

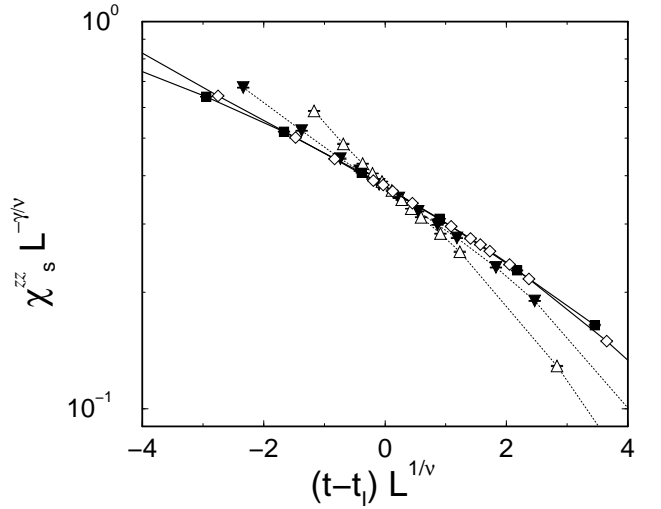


FIG. 9: Scaling plot for the longitudinal staggered susceptibility χ_s^{zz} in the EA model with $\Delta_\mu = 0.001$, for different L ; symbols as in Fig. 8. The universal scaling function emerges from the overlap of the two solid lines. The critical exponents $\gamma = 7/4$ and $\nu = 1$ are those of the Ising universality class, and the critical temperature is taken as $t_1 = 0.223$.

TABLE I: 2D Ising transition temperature $t_1(\Delta_\mu)$ as obtained by FSS analysis and fit of critical behaviours.

estimation method	$t_1(0.01)$	$t_1(0.001)$
$\xi^{zz} \sim L$	0.2815(25)	0.2225(15)
$U_4 \rightarrow 0.6107$	0.280(3)	
$M_s \sim L^{-\beta/\nu}$	0.282(2)	
$\chi_s^{zz} \sim L^{\gamma/\nu}$	0.2825(25)	0.2235(15)
$\xi^{zz} \sim t - t_1 ^{-\nu}$	0.283(6)	
$\chi_s^{zz} \sim t - t_1 ^{-\gamma}$	0.284(4)	

existence of an Ising phase transition is therefore given for both the considered anisotropies. Estimates of the critical temperature $t_1(\Delta_\mu)$ from the different criteria described in this section are summarized in Table I; all estimates are consistent, and amongst them we choose those realizing the best data collapse onto the universal scaling function in the scaling plots of staggered susceptibility and magnetization shown in Fig. 8 and 9: the resulting values are $t_1(0.01) = 0.281(2)$ and $t_1(0.001) = 0.223(2)$. Such values will be indicated with a thin arrow in the following figures.

B. Specific heat

The specific heat of the Ising model is characterized by a sharp peak at the transition temperature. As the anisotropy decreases, a large bump, eventually coinciding with the bump of the isotropic model, grows on the right-hand side of the peak, which correspondingly moves towards lower temperatures, meanwhile getting narrower.

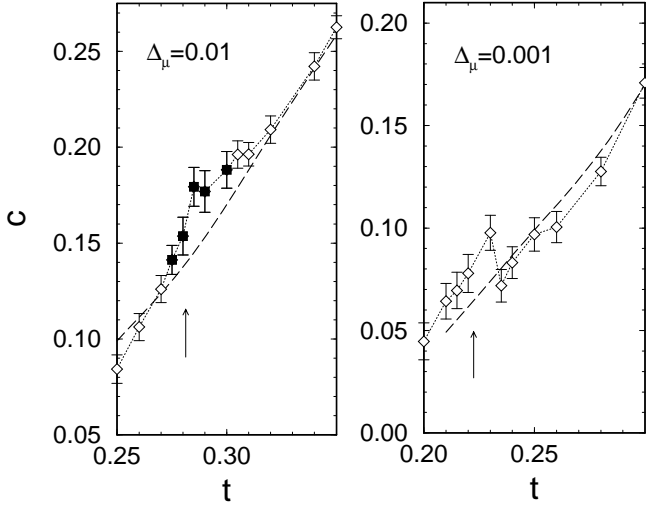


FIG. 10: Specific heat of the EA model vs t , for $L = 64$ (diamonds), and 128 (squares); the dashed line represent the specific heat of the isotropic model, as obtained by numerically deriving the internal energy QMC data of Ref. 46. Arrows indicate the estimated critical temperature.

In Fig. 10 we see that traces of an Ising-like peak emerging from the isotropic curve can still be evidenced for both anisotropy values. Despite their being traces, we observe that they develop at the critical temperature as estimated above. These findings are in good qualitative agreement with the experimental data⁴⁹ relative to the layered $S = 1/2$ antiferromagnet $\text{Cu}(\text{C}_5\text{H}_5\text{NO})_6(\text{BF}_4)_2$, which is supposed to have an anisotropy-driven transition; similar behaviour is displayed by larger-spin compounds whose anisotropy is known to be Ising-like⁵⁰, such as K_2NiF_4 ($S = 1$) and K_2MnF_4 ($S = 5/2$).

C. Uniform susceptibility

At variance with the specific heat, where the anisotropic curves just slightly differ from the isotropic one, the uniform susceptibility undoubtedly shows an anisotropic behaviour: in Fig. 11, where data relative to $\Delta_\mu = 0.01$ are shown, the transverse and longitudinal components, χ_u^{xx} and χ_u^{zz} , separate from the isotropic curve at $t \lesssim 0.4$, i.e., well above $t_1 = 0.282$. It is quite surprising that the Hamiltonian symmetry puts up so much resistance to the disordering effects of both quantum and thermal fluctuations: this means that the anisotropy, even as weak as those we are here considering, can never be neglected, and that there exists a temperature range, extending well above the transition (i.e., also out of the region where 2D correlations can trigger the onset of 3D long-range order), where genuinely 2D anisotropic behaviour can be experimentally observed.

The different temperature dependence of the transverse and longitudinal branches, with the former displaying a minimum and the latter monotonically going to

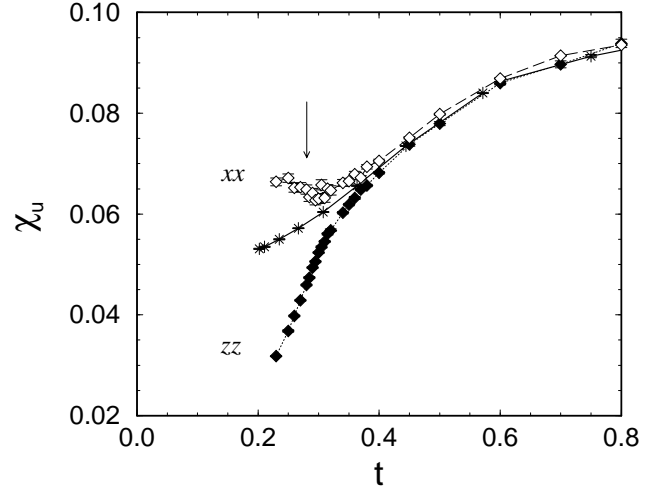


FIG. 11: Uniform susceptibility of the EA model for $\Delta_\mu = 0.01$ and $L = 64$. Full diamonds: longitudinal; open diamonds: transverse branch; stars: QMC data for the isotropic model⁴⁶. Solid and dashed lines are guides to the eye. The arrow indicates the estimated critical temperature.

zero, is that expected for an EA antiferromagnet. This behaviour results from the anisotropy-induced spin ordering, that makes the system more sensitive to the application of a transverse magnetic field, rather than of a longitudinal one. We observe that both the minimum of the in-plane component and the start of the rapid decrease of the longitudinal one, are close to the transition: as such feature is peculiar to the Ising model, this result gives further strength to the characterization of the transition as of Ising type.

The two components of the uniform susceptibility are experimentally observable by means of conventional magnetometry measurements: the above discussed deviations from the isotropic behaviour have been actually observed in several layered compounds with $S \geq 1$: K_2NiF_4 ⁵¹, Rb_2NiF_4 ⁵¹, BaNiF_4 ⁵² ($S = 1$), K_2MnF_4 ⁵³, Rb_2MnF_4 ⁵³, BaMnF_4 ⁵⁴ ($S = 5/2$). Such effects are here proved to be substantial also in $S = 1/2$ systems with a comparable anisotropy; unfortunately, to our knowledge, no clean experimental realization of a 2D $S = 1/2$ HAFM with small EA anisotropy is available yet.

D. Staggered susceptibility

The equal-time longitudinal and transverse staggered susceptibilities, χ_s^{zz} and χ_s^{xx} , for $\Delta_\mu = 0.01$ are shown in Fig. 12, together with the susceptibility of the isotropic model⁴⁶. Below the high-temperature region where the isotropic behaviour is reproduced, the two curves separate at $t \simeq 0.4$, below which χ_s^{zz} diverges more rapidly than in the isotropic case, while χ_s^{xx} stays finite and shows a maximum at about the transition temperature. The time-averaged susceptibilities display the same qual-

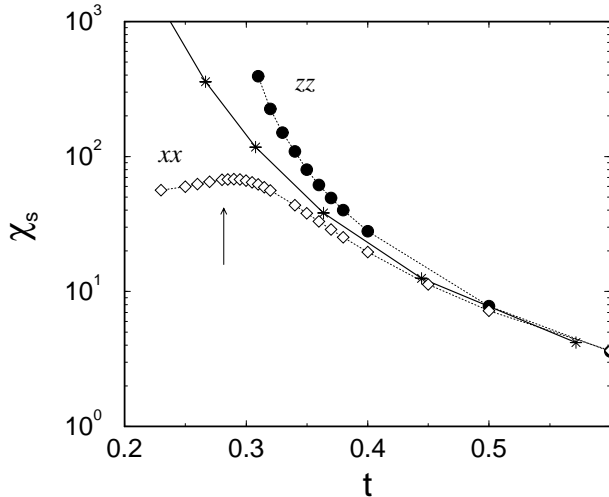


FIG. 12: Staggered susceptibility of the EA model for $\Delta_\mu = 0.01$. Circles: longitudinal (bulk values); diamonds: transverse ($L = 64$); stars, lines and arrow as in Fig. 11.

itative behaviour, though their values are slightly different with respect to the equal-time case.

As in the case of the uniform susceptibility, the observed behaviour is qualitatively suggestive of an Ising-like transition. Moreover, the analysis of longitudinal branch divergence gives a direct evidence of the Ising universality class, as well as an independent estimate of the critical temperature. For a 2D-Ising transition χ_s^{zz} must display a power-law divergence, $\chi_s^{zz} \sim |t - t_i|^{-\gamma}$, with $\gamma = 7/4$. In Fig. 14 we plot $(\chi_s^{zz})^{-1/\gamma}$ vs t for $\Delta_\mu = 0.01$, using data which are free of significant finite-size corrections, according to the criteria described in Section IV E. The power-law with the Ising exponent $\gamma = 7/4$ is evidently verified and the extrapolated critical temperature is $t_i = 0.284(4)$, which agrees with the more accurate value obtained in Section IV A. As for the smaller anisotropy, $\Delta_\mu = 0.001$, the power-law divergence of χ_s^{zz} could not be unambiguously detected for the considered lattice sizes.

E. Correlation length

Fig. 13 shows the longitudinal and the transverse correlation lengths, ξ^{zz} and ξ^{xx} , for $\Delta_\mu = 0.01$. The two correlation lengths behave quite differently: the transverse branch, after having left the longitudinal one at a temperature $t \simeq 0.4$, displays a maximum at the transition, while the longitudinal branch diverges faster than in the isotropic model. Again, the overall behaviour is suggestive of a 2D Ising transition.

The longitudinal antiferromagnetic correlation length ξ^{zz} is expected to display a power-law divergence $\xi^{zz} \sim |t - t_i|^{-\nu}$, with $\nu = 1$. One can capture this divergence by selecting a few points for ξ^{zz} at temperatures immediately above t_i , discarding those exceeding $L/4$, which are

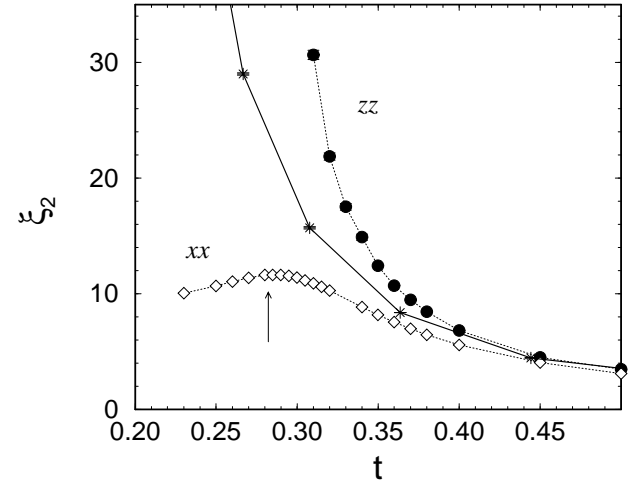


FIG. 13: Correlation length of the EA model for $\Delta_\mu = 0.01$. Symbols, lines and arrow as in Fig. 12.

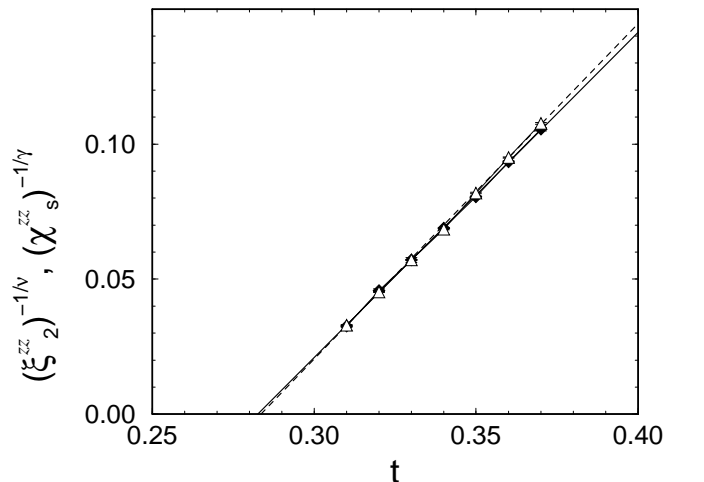


FIG. 14: Power-law critical behaviour of the longitudinal correlation length ξ^{zz} (diamonds) and of the longitudinal staggered susceptibility χ_s^{zz} (open triangles) for $\Delta_\mu = 0.01$; solid and dashed line are linear fits of $(\xi^{zz})^{-1/\nu}$ and $(\chi_s^{zz})^{-1/\gamma}$ respectively. The critical exponents $\nu = 1$ and $\gamma = 7/4$ are those of the Ising universality class.

affected by finite-size saturation. This criterion is reinforced by requiring the consistency of the estimates of ξ^{zz} obtained via the equal-time- and the time-averaged susceptibilities: since both estimates converge to the same value in the thermodynamic limit, their agreement indicates that finite-size effects are under control. For $\Delta_\mu = 0.01$, Fig. 14 shows that $(\xi^{zz})^{-1}$ is linear, with an extrapolated intercept $t_i = 0.283(6)$, in agreement with the value found via FSS analysis.

The same observation is not possible for $\Delta_\mu = 0.001$, as sizes larger than those here considered are required to approach the critical point of such model, while controlling finite-size effects.

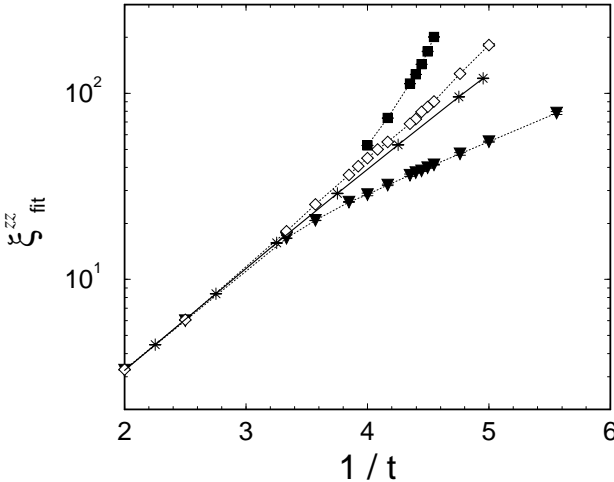


FIG. 15: Longitudinal correlation length ξ_{fit}^{zz} of the EA model with $\Delta_\mu = 0.001$, for $L = 32$ (down triangles), 64 (diamonds), 128 (squares). Stars and lines as in Fig. 11.

We have also extracted the longitudinal correlation length ξ^{zz} in the vicinity of the critical point by fitting the equal-time correlator $C^{zz}(\mathbf{r})$, defined in Eq. (21), to a function due to Serena, García and Levanyuk⁵⁵,

$$F(x) = \frac{e^{-x}}{x^{1/2} + x^{1/4}}, \quad (31)$$

properly symmetrized so as to take into account the periodic boundary conditions, i.e., by

$$C^{zz}(r) \propto F(r/\xi^{zz}) + F((L-r)/\xi^{zz}). \quad (32)$$

This function interpolates between the known asymptotic behaviours at $r \rightarrow 0$ and $r \rightarrow \infty$ of the Ising model. Well above the critical point we used the conventional fitting function for the isotropic antiferromagnet⁴⁴

$$F(x) = \frac{e^{-x}}{x^\eta}. \quad (33)$$

In the case $\Delta_\mu = 0.001$ good and stable fits are obtained even if the correlation length becomes comparable to (or even exceeds) the lattice size L : we can hence univocally define the fitted correlation length $\xi^{zz} \equiv \xi_{\text{fit}}^{zz}$. Moreover, the same kind of fitting procedure on the time-averaged correlator $C^{zz}(r)$, Eq. (21), gives consistent results.

Notice that ξ_{fit}^{zz} monotonically increases with L , bounded from above by the thermodynamic value; on the other hand, as ξ_{fit}^{zz} is systematically smaller than ξ^{zz} , the latter is necessarily less sensitive to size finiteness. For this reason it is possible to observe in Fig. 15 the clear deviation of ξ_{fit}^{zz} from the isotropic model, due to its divergence at t_i . To summarize, the sharp dependence of the longitudinal correlation length to small anisotropies, already observed for $S = 5/2$ in Rb_2MnF_4 ⁵⁶ and KFeF_4 ⁵⁷, is evidenced also for $S = 1/2$.

V. EASY-PLANE MODEL AND BKT TRANSITION

In this section we present our results relative to the EP model. We have used lattice sizes up to $L = 200$ and two anisotropy values: $\Delta_\lambda = 0.02$ (already considered in Ref. 10) and $\Delta_\lambda = 0.001$. These values are comparable with the experimentally estimated anisotropies of real compounds, amongst which several cupreous oxides such as La_2CuO_4 , $\text{Sr}_2\text{CuO}_2\text{Cl}_2$, and Pr_2CuO_4 , which are known to have an EP anisotropy³.

The temperature range covered by our simulations is $0.15 \lesssim t \lesssim 0.90$: as suggested by previous calculations^{7,10} this is the interval where we expect most of the peculiar features due to the anisotropy to be detectable. At higher temperatures the thermodynamic behaviour of the model does not differ from that of the isotropic one. On the other hand, finite-size limitations preclude the study of the very-low temperature region. To this respect, we recall that the correlation length of an EP model is expected to diverge exponentially as $t \rightarrow t_{\text{BKT}}^+$; such fast divergence makes finite-size limitations more severe than in the EA case, where ξ diverges algebraically. On the whole, the BKT transition offers less robust evidences, both numerically and experimentally, due to its being a topological phase transition rather than a second-order one.

In what follows we will refer to *out-of-plane* quantities as those related to the hard z -axis, and to *in-plane* quantities as those related to the easy xy -plane.

A. Finite-size scaling analysis

The role of the staggered magnetization in the FSS analysis of the EA behaviour is somehow taken, in the EP case, by the helicity modulus Υ , defined in Sec. III B. In the thermodynamic limit Υ is finite below and vanishes above the transition. When finite-size systems are considered, the occurrence of a BKT transition is marked by the existence of a finite temperature below which Υ scales to a finite value, as suggested by Fig. 16 for $\Delta_\lambda = 0.001$.

As for the value of the critical temperature, one knows that in the thermodynamic limit the ratio Υ/t gets the universal value $2/\pi$ at the transition⁵⁸. This behaviour is clearly detected in Fig. 17, where the helicity modulus is shown vs temperature for different L : the slope of $\Upsilon(t)$ near the point where the line $2t/\pi$ is crossed, gets larger for larger sizes, consistently with the occurrence of a jump in the thermodynamic limit.

An upper bound to the BKT critical temperature can be hence given by looking at the temperature t where the scaling behaviour of Υ/t is most compatible with the expected asymptotic value $2/\pi$ at criticality. From Fig. 16 we obtain $t_{\text{BKT}}(\Delta_\lambda=0.001) \lesssim 0.180$; the same procedure leads to $t_{\text{BKT}}(\Delta_\lambda=0.02) \lesssim 0.235$.

More accurate results are obtained by considering the critical scaling of Υ , Eq. (29). According to the procedure

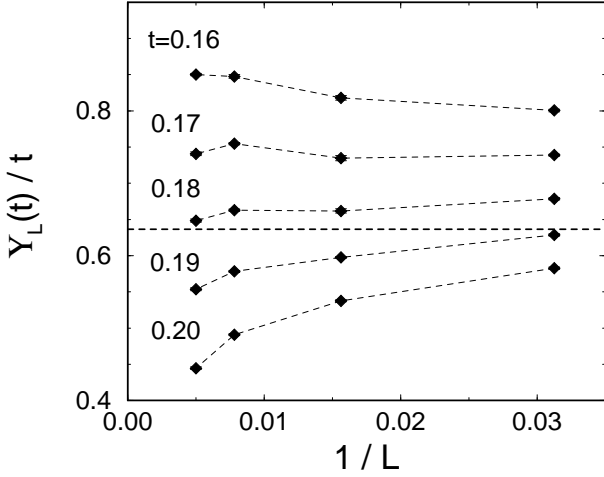


FIG. 16: Scaling of $\Upsilon_L(t)/t$ in the EP model for $\Delta_\lambda = 0.001$. The horizontal dashed line indicates the value $2/\pi$.

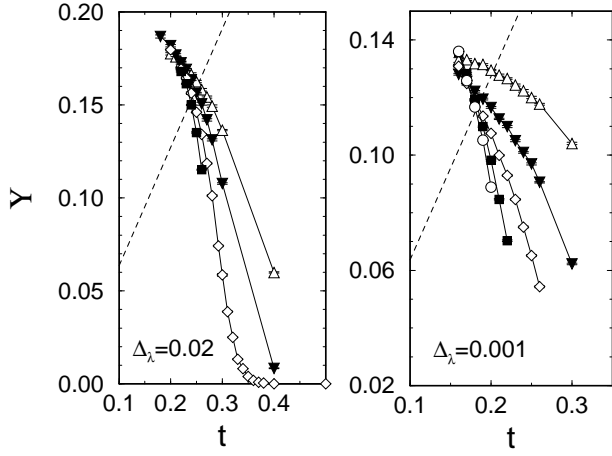


FIG. 17: Helicity modulus of the EP model for $L = 16$ (up triangles), 32 (down triangles), 64 (diamonds), 128 (squares), 200 (circles). The dashed line is the function $2t/\pi$.

suggested in Ref. 12, we assume the relation

$$\frac{\Upsilon_L(t)}{t} = \frac{2A(t)}{\pi} \left(1 + \frac{1}{2\log(L/L_0)} \right) \quad (34)$$

to hold in the vicinity of the transition; $A(t)$ and L_0 are then determined *via* a best-fit procedure and t_{BKT} identified as the temperature where $A(t)$ equals unity, as shown in Fig. 18. The resulting estimates are $t_{\text{BKT}}(\Delta_\lambda=0.02) = 0.229(2)$ and $t_{\text{BKT}}(\Delta_\lambda=0.001) = 0.172(5)$. In the case $\Delta_\lambda = 0.001$, this procedure is more uncertain: due to strong finite-size effects, Υ is seen to asymptotically scale just for $L \gtrsim 128$ (to be compared with $L \gtrsim 32$ in the case $\Delta_\lambda = 0.02$), so that the logarithmic fit can only be performed on two points ($L = 128, 200$) for each temperature.

There is another way to exploit the data for the helicity modulus of a finite-size system, though we are not aware of such technique having been used by other authors be-

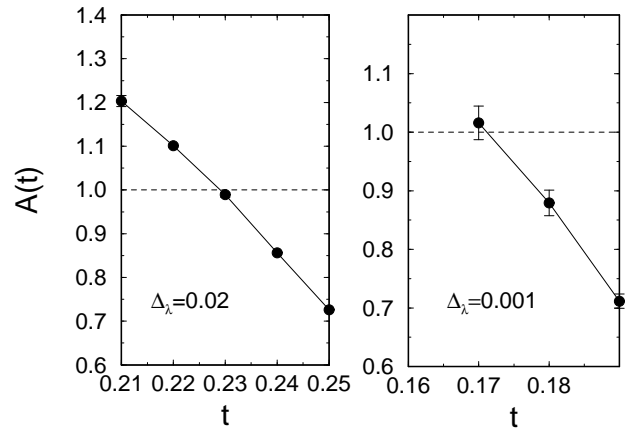


FIG. 18: Fitting parameter A vs t . The crossing point with the line $A = 1$ gives an estimate of the critical temperature t_{BKT} .

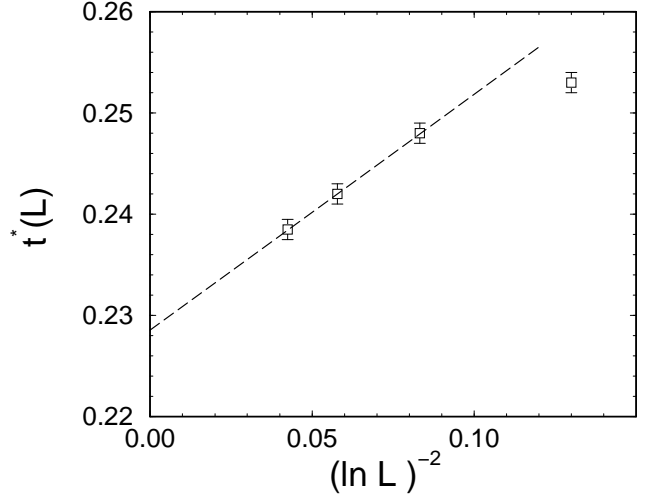


FIG. 19: Scaling of t^* with L for $\Delta_\lambda = 0.02$. The dashed line is a linear fit of the first three points, corresponding to $L = 32, 64, 128$.

fore. In Ref. 59, Bramwell and Holdsworth found that in the classical 2D planar-rotator model on a finite size the ratio Υ/t gets the universal value $2/\pi$ at a temperature $t^* > t_{\text{BKT}}$, whose size dependence is given by

$$t^* \simeq t_{\text{BKT}} + \frac{\pi^2}{4c(\ln L)^2} . \quad (35)$$

The above relation, determined by a renormalization-group based approach, is presented as a general property of BKT systems, though to our knowledge its validity has never been checked for models others than the classical pure planar one. On the other hand, in the case $\Delta_\lambda = 0.02$ we can easily determine t^* as a function of L from Fig. 17 and hence get Fig. 19, which shows that Eq. (35) holds even for weakly anisotropic, strongly quantum models; a linear fit of the scaling behaviour of t^* against $(\ln L)^2$ for $L \geq 32$ provides us

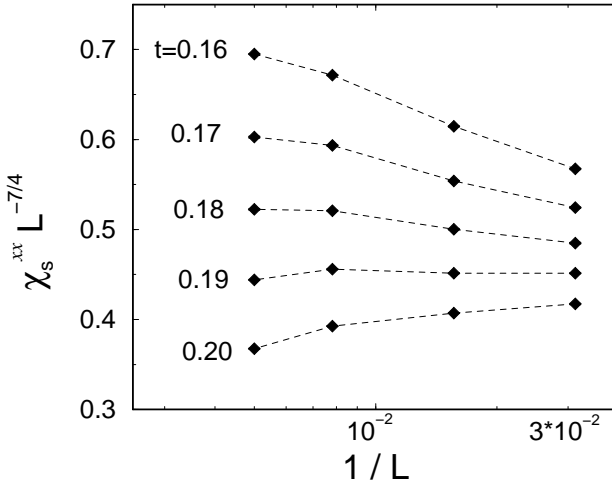


FIG. 20: Scaling of the in-plane staggered susceptibility χ_s^{xx} in the EP model with $\Delta_\lambda = 0.001$.

TABLE II: BKT transition temperatures $t_{\text{BKT}}(\Delta_\lambda)$ as obtained by FSS analysis and fit of critical behaviour of ξ^{xx} .

estimation method	$t_{\text{BKT}}(0.02)$	$t_{\text{BKT}}(0.001)$
asymptotic value of Υ	$\lesssim 0.235$	$\lesssim 0.175$
$A(t) = 1$	0.229(2)	0.172(5)
scaling of $t^*(L)$	0.228(4)	
$\chi_s^{xx} \sim L^{2-\eta}$	0.230(5)	0.180(5)
$\xi^{xx} \sim \exp[-b_\xi(t-t_{\text{BKT}})^{-1/2}]$	0.235(6)	

with a rather accurate estimate of the critical temperature, $t_{\text{BKT}}(\Delta_\lambda=0.02) = 0.228(4)$. Moreover, the results of Ref. 59 relate the coefficient c to the coefficient b_ξ appearing in Eq. (36) in the form $b_\xi = \pi/\sqrt{c}$, and from the linear fit we obtain $b_\xi = 0.96(9)$, in good agreement with the value obtained below by fitting the critical behaviour of the correlation length. This remarkably shows that the predictions of Ref. 59, derived for the classical 2D planar-rotator model, fully apply also to the quantum nearly-isotropic antiferromagnet we considered.

Finally, an additional estimate of the BKT critical temperature is obtained by the in-plane staggered susceptibility, which is expected to scale at the transition as $L^{2-\eta}$ with $\eta = 1/4$. Looking for the temperature where this scaling law is best verified, we obtain $t_{\text{BKT}}(\Delta_\lambda=0.02) = 0.230(5)$ and $t_{\text{BKT}}(\Delta_\lambda=0.001) = 0.180(5)$, as shown in Fig. 20 for the latter value.

Although the identification of the BKT universality class is less complete than in the Ising case, substantial consistence between the different estimates of the critical temperature obtained by different predictions of the Kosterlitz-Thouless theory proves that the two anisotropic models display a BKT critical regime. The estimates for the critical temperature $t_{\text{BKT}}(\Delta_\lambda)$ given in this section are summarized in Table II for the two anisotropies considered. Putting together these estimates

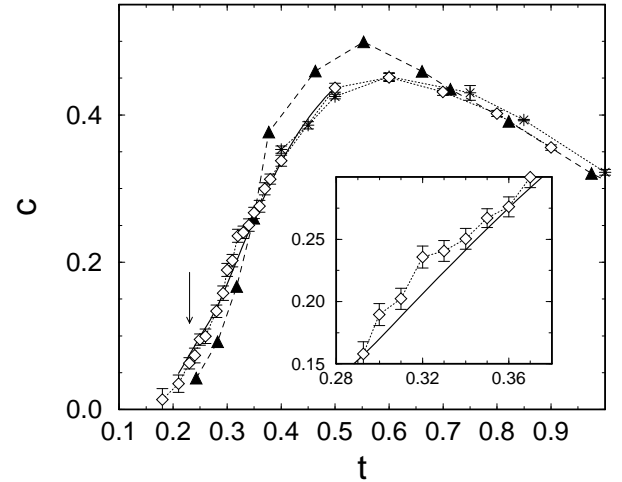


FIG. 21: Specific heat of the EP model with $\Delta_\lambda = 0.02$ for $L = 64$ (diamonds) compared to QMC data for the same model¹⁰ (triangles) and for the isotropic model^{44,46} (stars). The arrow indicates the estimated BKT temperature. Inset: zoom on the temperature region where a deviation is observed with respect to the isotropic case.

we choose as reference values $t_{\text{BKT}}(\Delta_\lambda=0.02) = 0.229(5)$ and $t_{\text{BKT}}(\Delta_\lambda=0.001) = 0.175(10)$. Such values will be indicated by a thin arrow in the figures of the following sections.

B. Specific heat

The specific heat does not show large systematic deviations from the isotropic case within the resolution reached by the simulations for both anisotropies considered. Only a small temperature region, well above the estimated transition temperature, displays an anomaly in the form of a tiny peak, as shown in Fig. 21; such peak is possibly reminiscent of the rounded peak shown by the specific heat of the quantum $S = 1/2$ XY model above its BKT transition¹¹. We must however mention that, at variance with our results, previous QMC data¹⁰, also reported in Fig. 21 significantly deviate from the isotropic model. According to the generally low sensitivity shown by the specific heat to weak anisotropies, as seen for instance in the EA case, we find this result a bit unlikely.

C. Uniform susceptibility

As in the EA case, the uniform susceptibility reported in Fig. 22 shows strong evidences of the anisotropy. Moving down from the high-temperature region, where the isotropic behaviour is reproduced, the in-plane χ_u^{xx} and out-of-plane χ_u^{zz} uniform susceptibilities separate from each other and from the isotropic data.

The in-plane component decreases faster than in the

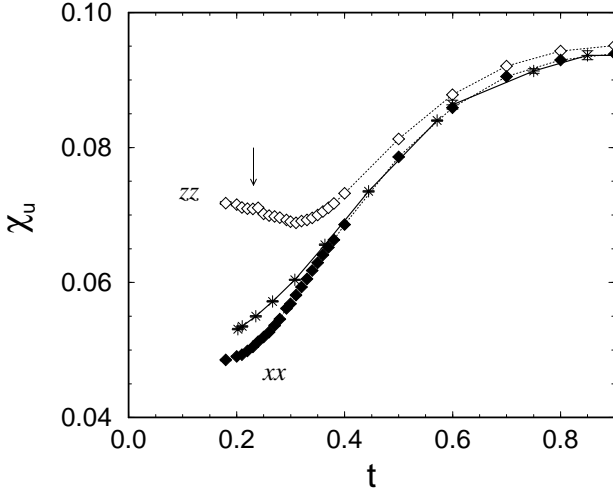


FIG. 22: Uniform susceptibility of the EP model with $\Delta_\lambda = 0.02$ and $L = 64$. Full diamonds: in-plane; open diamonds: out-of-plane; stars: QMC data for the isotropic model^{44,46}. Solid and dashed lines are guides to the eye. The arrow indicates the estimated BKT temperature.

isotropic case. At variance with the EA case, however, χ_u^{xx} is not expected to vanish at $t = 0$, due to the continuous rotational symmetry of the ground state in the xy plane. Indeed, in a semiclassical picture, such symmetry allows the staggered magnetization to align along the in-plane axis perpendicular to the field, making possible the canted spin configuration with a finite ferromagnetic magnetization parallel to -and linear in- the field, so that χ_u^{xx} stays finite.

The out-of-plane susceptibility is instead enhanced with respect to the isotropic case, showing a minimum well above the transition. Such minimum marks the onset of a completely different behaviour with respect to the isotropic model, entirely due to the presence of the small anisotropy.

D. Staggered susceptibility and correlation length

According to Kosterlitz theory⁴⁰, in presence of a BKT transition the correlation length ξ^{xx} is expected to diverge exponentially at finite temperature as

$$\xi^{xx} = a_\xi \exp [b_\xi (t - t_{\text{BKT}})^{-1/2}] . \quad (36)$$

As for the $\Delta_\lambda = 0.02$ model, this behaviour is in fact observed in Ref. 10, where it is used to estimate the critical temperature. We use the estimates ξ_{fit}^{xx} obtained by fitting the in-plane correlation function to Eqs. (32) and (33). Discarding the values affected by finite-size saturation and thus considering only those satisfying $\xi^{xx} \lesssim L/4$, we also observe the predicted behaviour: in particular, singling out the BKT critical region by successively dropping points at high temperature until a stable fit is obtained, we obtain $a_\xi = 0.6(2)$, $b_\xi = 1.0(1)$, and

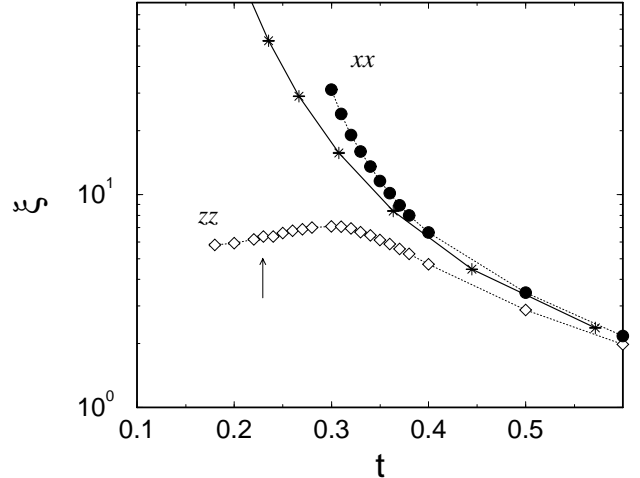


FIG. 23: Staggered correlation length of the EP model with $\Delta_\lambda = 0.02$. Circles: in-plane (bulk values); diamonds: out of plane ($L = 64$); dashed-line: BKT fit; stars, solid line and arrow as in Fig. 22.

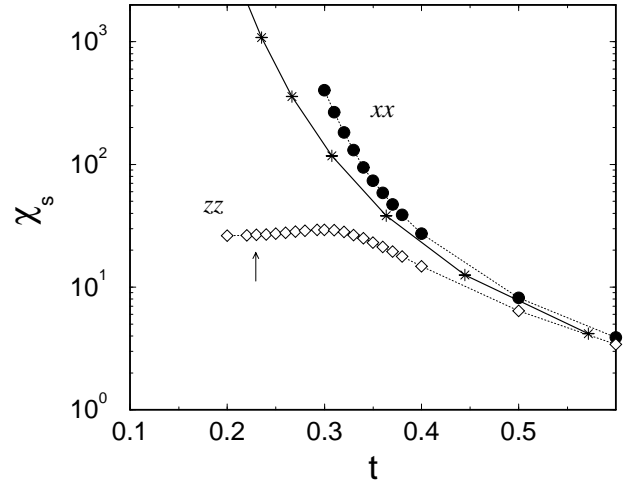


FIG. 24: Staggered susceptibility of the EP model with $\Delta_\lambda = 0.02$. Symbols as in Fig. 23; stars, lines and arrow as in Fig. 22.

the estimate $t_{\text{BKT}} = 0.235(6)$, which agrees with the value found via FSS analysis.

Furthermore, near criticality it is expected that the staggered in-plane susceptibility is related to the in-plane correlation length by the relation⁴⁰

$$\chi_s^{xx} = K (\xi^{xx})^{2-\eta} , \quad (37)$$

where K is a nonuniversal constant and $\eta = 1/4$. By plotting ξ_{fit}^{xx} together with $(\chi_s^{xx})^{1/(2-\eta)}$, as done in Fig. 25, one observes that this prediction also holds for the weakly-anisotropic quantum model; remarkably, the curve $(\chi_s^{xx})^{1/(2-\eta)}$ collapses onto the ξ^{xx} on a wide range of temperature so that $K \approx 1$: this property is not shared by, e.g., the classical planar rotator model or by the 2D

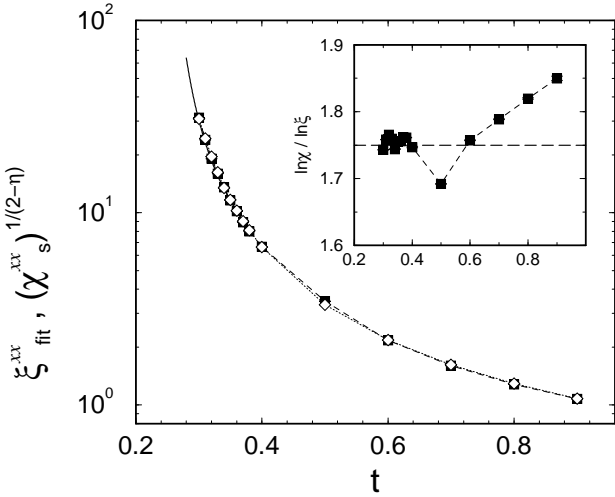


FIG. 25: Critical behaviour of $\xi_{\text{fit}}^{\text{xx}}$ (full squares) compared to that of $(\chi_s^{\text{xx}})^{1/(2-\eta)}$ with $\eta = 1/4$ (open diamonds) for the EP model with $\Delta_\lambda = 0.02$. The solid line is the BKT fit to the correlation length data. Inset: plot of $\ln \chi_s / \ln \xi$; the dashed line represents the expected BKT value $2 - \eta = 1.75$.

quantum XY model. A closer look to the validity of the scaling relation (37) can be obtained by plotting the ratio

$$\frac{\ln \chi_s^{\text{xx}}}{\ln \xi^{\text{xx}}} = 2 - \eta + \frac{\ln K}{\ln a_\xi + b_\xi(t - t_{\text{BKT}})^{-1/2}}, \quad (38)$$

which converges to the value $2 - \eta = 1.75$ when $t \rightarrow t_{\text{BKT}}^+$; this is clearly shown by the data plotted in the inset of Fig. 25.

In the $\Delta_\lambda = 0.001$ case, neither ξ_2^{xx} nor χ_s^{xx} exhibit the expected BKT critical behaviour for the considered lattice sizes. The correlation length obtained by fitting the correlator C^{xx} to the function (33) is also not of much help. This suggests the in-plane correlation length to behave as in the isotropic model up to relatively large values ($\xi^{\text{xx}} \approx 100$), and the same holds for the staggered susceptibility. Such findings closely resemble those of neutron scattering experiments on very weakly anisotropic layered $S = 1/2$ compounds, such as $\text{Sr}_2\text{CuO}_2\text{Cl}_2$ ⁶⁰, La_2CuO_4 ⁶¹ and Pr_2CuO_4 ⁶², that do not show signature of the existing anisotropy in the correlation length and static structure factor data.

Both the out-of-plane staggered susceptibility and correlation length have a non-critical behaviour, with a maximum well above the transition, at a temperature which roughly coincides with that of the minimum of the out-of-plane uniform susceptibility, marking the onset of an anisotropy-dominated regime. Both maxima are clearly decoupled from the transition temperature, at variance with the maximum of the transverse staggered susceptibility and correlation length observed in the EA case. To this respect we mention a definite disagreement with Ref. 10, where out-of-plane correlation length is conjectured to diverge exponentially when $T \rightarrow 0$. We show

such conjecture to be wrong, as ξ^{zz} is clearly seen to saturate to a finite value.

VI. PHASE DIAGRAM

The detailed analysis presented above for the EA and EP models separately, is now composed to form the phase diagram $t_{\text{I},\text{BKT}}$ vs $\Delta_{\mu,\lambda}$ in Fig. 26, where our best estimates for the critical temperatures relative to the four models considered are shown, together with data from Refs. 9 and 10. Critical temperatures are seen to be strongly reduced with respect to the classical values, as given for instance in Ref. 7: however, the diagram clearly suggests the critical temperatures to stay finite for any finite anisotropy, both in the EA and in the EP case, thus leading to the conclusion that quantum fluctuations cannot destroy the transition.

We can actually see that the above conclusion is the consequence of a more general finding. If one numerically analyses $t_{\text{I},\text{BKT}}(\Delta_{\mu,\lambda})$ finds that a logarithmic dependence is well consistent with our data, as shown in Fig. 26. Such dependence, already predicted by renormalization group techniques^{5,19}, is rederived in Appendix C on the basis of a fully classical argument. It is found that

$$T_{\text{I}} \approx \frac{4\pi\rho_s}{\ln(c/\Delta_\mu)}, \quad (39)$$

and

$$T_{\text{BKT}} \approx \frac{4\pi\rho_s}{\ln(c'/\Delta_\lambda)}. \quad (40)$$

where c and c' are constants depending on the specific model considered, while ρ_s is the spin stiffness of the classical isotropic model, entering the above expressions via the exponential divergence of its correlation length. The dominant effect of quantum fluctuations on such divergence is embodied in the spin stiffness renormalization; therefore, if the ordering process we are here observing is the same as in the classical case, we expect $4\pi\rho_s = 2.26 J$, where the value $\rho_s = 0.18 J$ has been taken for the renormalized $S = 1/2$ isotropic spin stiffness⁴⁵. From the logarithmic fits of the quantum data we indeed find 2.22 and 2.49 as prefactors of the logarithm, which are remarkably near to the predicted value, despite the simplicity of the argument that led to it.

For $\Delta_\lambda = 0.02$ and $\Delta_\mu = 0.01$, where a direct comparison is possible, the critical temperatures are not fully consistent with the values given in Refs. 9 and 10. We notice that the latter were estimated as free parameters of fitting functions for the critical behaviour of the susceptibility and correlation length; the precision of this approach is hindered by the fact that the critical regime of both quantities was not always properly entered in the simulations of Refs. 9 and 10, mainly due to technical limitations which are nowadays overcome. We therefore propose our data as more precise estimates.

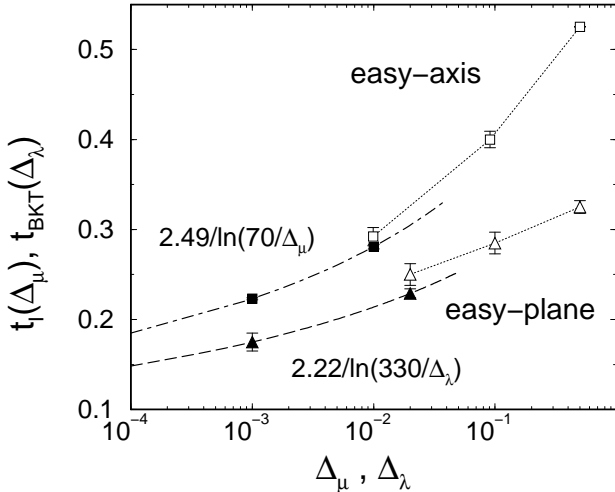


FIG. 26: Phase diagram of the $S = 1/2$ 2d XXZ model on the square lattice for weak anisotropies. Full symbols are results of this work, open symbols are QMC data from Refs. 9 and 10.

VII. CONCLUSIONS

In this paper we have presented an extensive numerical study of thermodynamic and critical properties of weakly anisotropic two-dimensional quantum antiferromagnets described by the 2D $S = 1/2$ XXZ model with both EA and EP anisotropy. Use has been made of the continuous-time QMC method based on the loop algorithm, implemented here for the first time also in the EA case, and on the worm algorithm, here reformulated as a variant of the loop algorithm.

The general outcome of the numerical simulations is that the thermodynamics of 2D quantum antiferromagnets is extremely sensitive to the presence of anisotropies of magnitude comparable to those of real compounds, i.e., as small as 10^{-3} times the dominant isotropic coupling.

In the models studied we see a finite temperature transition to persist with clear signatures of Ising and BKT critical behaviour, in the EA and EP case, respectively; in the more anisotropic case (10^{-2}) full consistency with the expected universality class is found. The most striking evidences of the presence of the exchange anisotropy are observed in the thermodynamic behaviour of correlation lengths and susceptibilities. Moreover, the dependence of the critical temperature on the anisotropy is found to be quantitatively consistent with the prediction relative to the classical case, with properly renormalized parameters. This tells us that quantum effects can neither destroy the transition, nor change the ordering mechanism responsible for the transition to occur and that our quantum models, despite having $S = 1/2$ and very weak anisotropies, do actually behave as renormalized classical ones. Given the results of Ref. 7 for $S \geq 1$, we can say that this conclusion generally holds for quantum Heisenberg antiferromagnets on the square lattice.

As for the thermodynamic behaviour of the specific

observables considered, we find all the non-diverging quantities to be highly sensitive to the anisotropy, while critical quantities show deviations, with respect to the isotropic case, which are generally harder to detect. This is due to the fact that, in order to discriminate between $T = 0$ isotropic and finite- T anisotropic divergences one must come very close to the critical point of the anisotropic model, which is a non-trivial issue both numerically (due to severe finite-size effects) and experimentally (due to finite experimental resolution and intralayer coupling).

As for the EP case, we underline that the considered values of anisotropy compare to that of several real compounds. On the other hand, we have clearly shown, for instance in Figs. 22, 23 and 24, that in the EP case traces of 2D anisotropic behaviour are detectable above the transition, due to the fact that some quantities display either a minimum or a maximum in a temperature region well apart from t_{BKT} , where the in-plane correlation length has not diverged yet, and experimental observation should hence be more feasible. We therefore think that our results could constitute a sound basis for a possible experimental observation of genuinely 2D EP behaviour in real magnets.

Acknowledgments

The numerical calculations which led to the present work have been performed on the parallel cluster at CILEA (Milano, Italy), on the beowulf cluster CINECA (Bologna, Italy) through INFM grant no. 1114174655, on the beowulf cluster at INOA (Firenze, Italy) and on the PC's of the Institut für theoretische Physik at the University of Leipzig (Germany). We thank all these institutions for their generous support. We thank T. Sauer and W. Janke for participation to the early stage of this project. T.R. acknowledges fruitful conversations with B.B. Beard, N. Kawashima, P. Carretta and M. Laurati. T.R. further acknowledges the Institut für theoretische Physik at Leipzig University for hospitality during the early steps of this project, and CRUI for financial support via the VIGONI programme. This work has been partially supported by the COFIN2000-MURST fund.

APPENDIX A: ISING LIMIT OF THE WORM ALGORITHM

We show that the Ising limit of the worm algorithm is nothing but the standard single-flip Metropolis algorithm, considering the simple case of an Ising antiferromagnetic spin dimer. Independent transitions via single spin flip are only two: (i) $|\uparrow\uparrow\rangle \rightarrow |\downarrow\uparrow\rangle$ and (ii) its reversal. Within the worm algorithm, the transition (i) occurs with probability 1, since the spin configuration $|\uparrow\uparrow\rangle$ admits no bounce; this equals the Metropolis result, since a net energy gain $J^Z/2$ is obtained in the process

(i). Starting from the configuration $|\downarrow\uparrow\rangle$ a bounce process is instead possible with a probability per unit time $\pi(3, b) = J^Z/2$; if the worm experiences even a single bounce, it will u-turn finding on its way back only plaquettes of type 1(2), on which it cannot bounce, until it reaches its tail leaving the configuration unchanged. Therefore the transition occurs with probability $1 - p_{1b}$, where p_{1b} is the probability of experiencing at least one bounce. Since the number of bounces follows a Poisson distribution with parameter $\beta\pi(3, b)$, we have that

$$1 - p_{1b} = 1 - \sum_{k \geq 1} \frac{[\beta\pi(3, b)]^k}{k!} e^{-\beta\pi(3, b)} = e^{-\beta J^Z/2} \quad (\text{A1})$$

which is exactly the Metropolis transition probability for a process involving an energy increase $J^Z/2$.

APPENDIX B: ESTIMATOR OF THE HELICITY MODULUS

In this section we derive the QMC estimator (27) for the helicity modulus starting from its thermodynamic definition (26). The derivation is a finite-temperature generalization of the one given by Sandvik in Ref. 63, in the context of Stochastic Series Expansion, to estimate the spin stiffness, i.e., at zero temperature.

We start from the "twisted" XXZ hamiltonian, with the twist applied along the 1-direction of the lattice, as:

$$\begin{aligned} \hat{\mathcal{H}}(\phi) = & \sum_i [J^{XY} \cos \phi (\hat{S}_i^x \hat{S}_{i+d_1}^x + \hat{S}_i^y \hat{S}_{i+d_1}^y) \\ & + J^{XY} \sin \phi (\hat{S}_i^x \hat{S}_{i+d_1}^y - \hat{S}_i^y \hat{S}_{i+d_1}^x) + J^Z \hat{S}_i^z \hat{S}_{i+d_1}^z] \\ & + \hat{\mathcal{H}}_2 \end{aligned} \quad (\text{B1})$$

where $\mathbf{d}_1 = (1, 0)$ and $\hat{\mathcal{H}}_2$ is the term containing only bonds along the 2-direction, which remains unchanged.

We expand the twisted Hamiltonian to second order in ϕ as:

$$\hat{\mathcal{H}}(\phi) = \hat{\mathcal{H}}(\phi = 0) - \phi \hat{\mathcal{J}}_1 - \frac{\phi^2}{2} \hat{\mathcal{H}}_1^{(XY)} + \mathcal{O}(\phi^3) \quad (\text{B2})$$

where

$$\hat{\mathcal{J}}_1 = \frac{i J^{XY}}{2} \sum_i (\hat{S}_i^+ \hat{S}_{i+d_1}^- - \hat{S}_i^- \hat{S}_{i+d_1}^+) \quad (\text{B3})$$

is the 1-component of the spin current operator, and

$$\hat{\mathcal{H}}_1^{(XY)} = \frac{J^{XY}}{2} \sum_i (\hat{S}_i^+ \hat{S}_{i+d_1}^- + \hat{S}_i^- \hat{S}_{i+d_1}^+) \quad (\text{B4})$$

Carefully deriving the free energy with respect to the twist, i.e., taking care of the non-commutativity between the $\hat{\mathcal{H}}(\phi = 0)$, $\hat{\mathcal{J}}_1$ and $\hat{\mathcal{H}}_1^{(XY)}$ operator, one obtains for the helicity modulus, averaged over the 1- and 2-direction of the applied twist, the expression:

$$\Upsilon = -\frac{1}{2 J^{XY} L^2} \left(\langle \hat{\mathcal{H}}^{(XY)} \rangle + \int_0^\beta d\tau \langle \hat{\mathbf{J}}(0) \cdot \hat{\mathbf{J}}(\tau) \rangle \right) \quad (\text{B5})$$

where $\hat{\mathcal{H}}^{(XY)} = \hat{\mathcal{H}}_1^{(XY)} + \hat{\mathcal{H}}_2^{(XY)}$ and $\hat{\mathbf{J}} = (\hat{\mathcal{J}}_1, \hat{\mathcal{J}}_2)$. Such expression stands as the direct quantum analogue of the classical expression as given in, e.g., Ref. 64 for the plane rotator model; in the limit of zero temperature it reproduces the expression given by Ref. 63.

The QMC estimator (27) can be obtained directly starting from (B5) in the case $S = 1/2$. In the continuous-time limit, the estimator for the bond exchange operators $\hat{T}_{i\mathbf{d}_1}^\pm = (J^{XY}/2) \hat{S}_i^\pm \hat{S}_{i+d_1}^\mp$ takes the form:

$$\langle \hat{T}_{i\mathbf{d}_1}^\pm \rangle = \frac{1}{\beta} \int_0^\beta d\tau \langle \hat{T}_{i\mathbf{d}_1}^\pm(\tau) \rangle = -\frac{1}{\beta} \langle N_{i\mathbf{d}_1}^\pm \rangle_{\text{MC}} \quad (\text{B6})$$

where $N_{i\mathbf{d}_1}^+$ is the number of (+)-kinks (of the type $|\downarrow i \uparrow i+d_1\rangle \rightarrow |\uparrow i \downarrow i+d_1\rangle$) on the $i, i+d_1$ bond, and analogously for $N_{i\mathbf{d}_1}^-$. Therefore the estimator for the XY-energy takes the form:

$$\langle \hat{\mathcal{H}}^{(XY)} \rangle = -\frac{1}{\beta} \langle N^+ + N^- \rangle_{\text{MC}} \quad (\text{B7})$$

where N^\pm is the total number of (\pm)-kinks present in each configuration. The current-current correlator present in (B5) can be decomposed into bond-pair contributions as follows:

$$\hat{\mathcal{J}}_1(0) \hat{\mathcal{J}}_1(\tau) = - \sum_{i,j} [\hat{T}_{i\mathbf{d}_1}^+(0) - \hat{T}_{i\mathbf{d}_1}^-(0)] [\hat{T}_{j\mathbf{d}_1}^+(\tau) - \hat{T}_{j\mathbf{d}_1}^-(\tau)] \quad (\text{B8})$$

Taking into account the $S=1/2$ constraint $\hat{S}^\pm \hat{S}^\pm |\sigma\rangle = 0$, one obtains that

$$\begin{aligned} & \int_0^\beta d\tau \langle [\hat{T}_{i\mathbf{d}_1}^+(0) - \hat{T}_{i\mathbf{d}_1}^-(0)] [\hat{T}_{j\mathbf{d}_1}^+(\tau) - \hat{T}_{j\mathbf{d}_1}^-(\tau)] \rangle = \\ & = \frac{1}{\beta} \left[\langle (N_{i\mathbf{d}_1}^+ - N_{i\mathbf{d}_1}^-)(N_{j\mathbf{d}_1}^+ - N_{j\mathbf{d}_1}^-) \rangle_{\text{MC}} \right. \\ & \quad \left. - \delta_{ij} \langle (N_{i\mathbf{d}_1}^+ + N_{i\mathbf{d}_1}^-) \rangle_{\text{MC}} \right] \quad (\text{B9}) \end{aligned}$$

Putting together (B7) and (B9) with (B5) one obtains:

$$\Upsilon = \frac{t}{2L^2} \left\langle (N_1^+ - N_1^-)^2 + (N_2^+ - N_2^-)^2 \right\rangle_{\text{MC}} \quad (\text{B10})$$

where $(N_{1(2)}^\pm)$ is the total number of \pm -kinks on 1(2)-bonds. Since a (+)-kink and a (-)-kink affect a spin path crossing the kink by shifting it of a lattice spacing in opposite directions, we have that the spin-path winding number can be expressed as

$$W_{1(2)} = (N_{1(2)}^+ - N_{1(2)}^-)/L \quad (\text{B11})$$

and this reduces the estimator (B10) to the expression (27).

APPENDIX C: CLASSICAL DESCRIPTION OF THE ORDERING MECHANISM

We give here a sketchy description of the ordering mechanism in slightly anisotropic 2D magnets, referring

to the classical limit where the antiferro- and ferromagnetic cases are thermodynamically equivalent.

EA case. We rewrite the Hamiltonian (1) in the classical limit as

$$\begin{aligned}\mathcal{H} &= -\frac{J_{\text{cl}}}{2} \sum_{\mathbf{i}, \mathbf{d}} \mathbf{s}_{\mathbf{i}} \cdot \mathbf{s}_{\mathbf{i}+\mathbf{d}} + \mathcal{H}' \\ \mathcal{H}' &= \frac{J_{\text{cl}} \Delta_{\mu}}{2} \sum_{\mathbf{i}, \mathbf{d}} (s_{\mathbf{i}}^x s_{\mathbf{i}+\mathbf{d}}^x + s_{\mathbf{i}}^y s_{\mathbf{i}+\mathbf{d}}^y)\end{aligned}\quad (\text{C1})$$

where $\mathbf{s} = (\cos \theta \sin \phi, \sin \theta \sin \phi, \cos \theta)$ is a unitary classical vector and J_{cl} is the classical exchange constant. In the above form the Hamiltonian is written as the isotropic Heisenberg Hamiltonian plus, as long as $\Delta_{\mu} \ll 1$, a small Ising perturbation \mathcal{H}' . The isotropic Heisenberg model has an exponentially divergent correlation length as $T \rightarrow 0^{65}$, $\xi \approx aT e^{2\pi\rho_s/T}$, where ρ_s is the spin stiffness of the classical model. At very high temperatures, i.e., $T \gg J_{\text{cl}}$, the spins are fully uncorrelated, so that the anisotropy has little effect. When $T \approx J_{\text{cl}}$ correlations set on and clusters of almost aligned spins form on the length scale ξ . Very roughly, one can imagine the ξ^2 spins of each cluster C to be fully aligned, so that the anisotropy term can be written as

$$\begin{aligned}\mathcal{H}' &= \frac{J_{\text{cl}} \Delta_{\mu}}{2} \sum_{\mathbf{i}, \mathbf{d}} \cos(\phi_{\mathbf{i}} - \phi_{\mathbf{i}+\mathbf{d}}) \sin \theta_{\mathbf{i}} \sin \theta_{\mathbf{i}+\mathbf{d}} \\ &\approx J_{\text{cl}} \Delta_{\mu} \xi^2 \sum_C \sin^2 \theta_C,\end{aligned}\quad (\text{C2})$$

where θ_C is the polar angle of the spin orientation on each cluster and border terms of order ξ are neglected. Hence, the anisotropy term creates an effective potential for the orientation of each correlated cluster that has two minima in $\theta_C = 0$ and π (up and down) separated by

an energy barrier $\Delta E = J_{\text{cl}} \Delta_{\mu} \xi^2$. When ξ increases upon lowering T , the barrier becomes comparable to the thermal energy, so that the orientation of each cluster is confined to one side of the potential barrier: the system becomes Ising-like and a finite magnetization appears. Using the isotropic behaviour of ξ , this happens when

$$T \approx \Delta E = J_{\text{cl}} \Delta_{\mu} (aT e^{2\pi\rho_s/T})^2; \quad (\text{C3})$$

solving this equation gives the critical temperature as in Eq. (39).

The above simplified picture accounts for the logarithmic dependence of T_c upon the (small) anisotropy Δ_{μ} that was earlier obtained via more sophisticated approaches⁶⁶; the logarithm appears to follow from the exponential correlation length in the isotropic model.

EP case. The above argument can be essentially rephrased, this time taking as perturbation of the isotropic Hamiltonian the term

$$\mathcal{H}' = \frac{J_{\text{cl}} \Delta_{\lambda}}{2} \sum_{\mathbf{i}, \mathbf{d}} s_{\mathbf{i}}^z s_{\mathbf{i}+\mathbf{d}}^z, \quad (\text{C4})$$

which, in presence of clusters on the scale ξ , becomes

$$\mathcal{H}' \approx J_{\text{cl}} \Delta_{\lambda} \xi^2 \sum_C \cos^2 \theta_C. \quad (\text{C5})$$

The anisotropy potential has the minimum at $\theta_C = \pi/2$, i.e., for a cluster orientation on the xy -plane, and the well depth is $\Delta E = J_{\text{cl}} \Delta_{\lambda} \xi^2$. As in the EA case, the anisotropy becomes relevant once T is comparable to ΔE : the out-of-plane fluctuations are suppressed making the system effectively planar, so that vortex excitations appear and the BKT transition can take place. This roughly happens when Eq. (40) holds.

¹ *Magnetic Properties of Layered Transition Metal Compounds*, edited by L. J. de Jongh (Kluwer, Dordrecht, 1990).
² E. Manousakis, Rev. Mod. Phys. **63**, 1 (1991).
³ D. C. Johnston, in *Handbook of Magnetic Materials*, vol. **10**, edited by K. H. J. Buschow (Elsevier Science, New York, 1997), page 1.
⁴ A. Drzewinski and J. Sznajd, Phys. Lett. A **138**, 143 (1989).
⁵ V. Yu. Irkhin and A. A. Katanin, Phys. Rev. B **57**, 379 (1998); Phys. Rev. B **60**, 2990 (1999).
⁶ A. Cuccoli, V. Tognetti, P. Verrucchi, and R. Vaia, Phys. Rev. B **51**, 12840 (1995); L. Capriotti, A. Cuccoli, V. Tognetti, P. Verrucchi, and R. Vaia, Physica D **119**, 68 (1998); A. Cuccoli, T. Roscilde, V. Tognetti, P. Verrucchi, and R. Vaia, Phys. Rev. B **62**, 3771 (2000).
⁷ A. Cuccoli, T. Roscilde, V. Tognetti, P. Verrucchi, and R. Vaia, Eur. Phys. J. B **20**, 55 (2001).
⁸ S. S. Aplesnin, J. Phys.: Condens. Matt. **10**, 10061 (1998); Phys. Stat. Sol. (b) **207**, 491 (1998).

⁹ H.-Q. Ding, J. Phys.: Condens. Matt. **2**, 7979 (1990);
¹⁰ H.-Q. Ding, Phys. Rev. Lett. **68**, 1927 (1992).
¹¹ H.-Q. Ding, Phys. Rev. B **45**, 230 (1992).
¹² K. Harada and N. Kawashima, J. Phys. Soc. Jpn. **67**, 2768 (1998).
¹³ L. J. de Jongh, in Ref. 1, page 1.
¹⁴ S. Hikami and T. Tsuneto, Progr. Theor. Phys. **63**, 387 (1980).
¹⁵ S. T. Bramwell and P. C. W. Holdsworth, J. Appl. Phys. **73**, 6096 (1993).
¹⁶ K. Kubo and T. Kishi, Phys. Rev. Lett. **61**, 2585 (1988).
¹⁷ H.-A. Wischmann and E. Müller-Hartmann, J. Phys. I (France) **1**, 647 (1991).
¹⁸ J. D. Reger and A. P. Young, Phys. Rev. B **37**, 5978 (1988); T. Barnes, D. Kotchan and E. S. Swanson, Phys. Rev. B **39**, 4357 (1989); H.-Q. Lin, J. S. Flynn and D. D. Betts, Phys. Rev. B **64**, 214411 (1999).
¹⁹ S. B. Khokhlocev, Sov. Phys. JETP **43**, 137 (1976).
²⁰ J. Fröhlich and E. H. Lieb, Phys. Rev. Lett. **38**, 440 (1977).
²¹ F. Dunlop, J. Stat. Phys. **41**, 733 (1985).

²² N. S. Branco and J. R. de Sousa, Phys. Rev. B **62**, 5742 (2000).

²³ J. R. de Sousa and I. G. Araújo, Phys. Lett. A **272**, 333 (2000).

²⁴ M. Suzuki, Progr. Theor. Phys. **56**, 1454 (1976); M. Barma and B. S. Shastry, Phys. Rev. B **18**, 3351 (1978).

²⁵ H. G. Evertz, G. Lana and M. Marcu, Phys. Rev. Lett. **70**, 875 (1993); H. G. Evertz, *The Loop Algorithm*, in *Numerical Methods for Lattice Quantum Many-Body Problems*, edited by D. J. Scalapino, (Perseus Book, Frontiers in Physics, Reading, 2001).

²⁶ The weight of plaquette configurations of type 1 (2) differ from those given in Eq.(36) of Ref. 25 as we did not multiply by the arbitrary factor $\exp(-\frac{J^2}{4}\Delta\tau)$; this also affects the break-up weights given in Eqs. (6) and (7).

²⁷ J. J. Cullen and D. P. Landau, Phys. Rev. B **27**, 297 (1983).

²⁸ R. H. Swendsen and J.-S. Wang, Phys. Rev. Lett. **58**, 86 (1987).

²⁹ U. Wolff, Phys. Rev. Lett. **62**, 361 (1989); Nucl. Phys. B **334**, 581 (1990).

³⁰ B. B. Beard and U.-J. Wiese, Phys. Rev. Lett. **77**, 5130 (1996).

³¹ R. Brower, S. Chandrasekharan, and U.-J. Wiese, Physica A **261**, 520 (1998).

³² J. V. Alvarez and C. Gros, Eur. Phys. J. B **15**, 641 (2000).

³³ N. V. Prokofev, B. V. Svistunov, and I. S. Tupitsyn, Pis'ma Zh. Eksp. Teor. Fiz. **64**, 853 (1996) [JETP Lett. **64**, 911 (1996)]; Phys. Lett. A **238**, 253 (1998); Zh. Eksp. Teor. Fiz. **114**, 570 (1998) [J. Exp. Theor. Phys. **87**, 310 (1998)].

³⁴ A. W. Sandvik, Phys. Rev. B **59**, R14157 (1999).

³⁵ H. Onishi, M. Nishino, N. Kawashima, and S. Miyashita, J. Phys. Soc. Jpn. **68**, 2547 (1999).

³⁶ F. Cooper, B. Freedman, and D. Preston, Nucl. Phys. **B210**, 210 (1982).

³⁷ E. L. Pollock and D. M. Ceperley, Phys. Rev. B **36**, 8343 (1987).

³⁸ M. N. Barber, in *Phase Transitions and Critical Phenomena*, vol. **8**, edited by C. Domb and J. L. Lebowitz, (Academic, London, 1983).

³⁹ See, e.g., S. Caracciolo, A. Gambassi, M. Gubinelli, and A. Pelissetto, Eur. Phys. J. B **20**, 255 (2001), and references therein.

⁴⁰ J. M. Kosterlitz, J. Phys. C **7**, 1046 (1974).

⁴¹ P. Olsson and P. Minnhagen, Physica Scripta **43**, 203 (1991).

⁴² H. Weber and P. Minnhagen, Phys. Rev. B **37**, 5986 (1988).

⁴³ P. Olsson, Phys. Rev. B **52**, 4526 (1995).

⁴⁴ M. S. Makivić and H.-Q. Ding, Phys. Rev. B **43**, 3562 (1991).

⁴⁵ B. B. Beard, R. J. Birgeneau, M. Greven, and U.-J. Wiese, Phys. Rev. Lett. **80**, 1742 (1998).

⁴⁶ J.-K. Kim and M. Troyer, Phys. Rev. Lett. **80**, 2705 (1998).

⁴⁷ K. Binder, Z. Phys. B **43**, 119 (1981).

⁴⁸ G. Kamieniarz and H. W. J. Blöte, J. Phys. A: Math. Gen. **26**, 201 (1993).

⁴⁹ H. A. Algra, L. J. de Jongh, and R. L. Carlin, Physica **93B**, 24 (1978).

⁵⁰ M. B. Salamon and H. Ikeda, Phys. Rev. B **7**, 2017 (1973); I. Hatta and H. Ikeda, J. Phys. Soc. Jpn. **48**, 77 (1980).

⁵¹ M. Matsuura, K. Gillijamse, J. E. W. Sterkenburg, and D. J. Breed, Phys. Lett. **33A**, 363 (1970).

⁵² D. E. Cox, M. Eibschutz, H. J. Guggenheim, and L. Holmes, J. Appl. Phys. **41**, 943 (1970).

⁵³ D. J. Breed, Phys. Lett. **23**, 181 (1966); Physica **37**, 35 (1967).

⁵⁴ L. Holmes, M. Eibschutz, and H. J. Guggenheim, Sol. St. Comm. **7**, 973 (1969).

⁵⁵ P. A. Serena, N. García, and A. Levanyuk, Phys. Rev. B **47**, 5027 (1993).

⁵⁶ Y. S. Lee, M. Greven, B. O. Wells, R. J. Birgeneau, and G. Shirane, Eur. Phys. J. B **5**, 15 (1998).

⁵⁷ S. Fulton, R. A. Cowley, A. Desert, and T. Mason, J. Phys.: Condens. Matt. **6**, 6679 (1994).

⁵⁸ D. R. Nelson and J. M. Kosterlitz, Phys. Rev. Lett. **39**, 1201 (1977).

⁵⁹ S. T. Bramwell and P. C. W. Holdsworth, J. Phys.: Condens. Matt. **5**, L53 (1993).

⁶⁰ M. Greven, R. J. Birgeneau, Y. Endoh, M. A. Kastner, M. Matsuda, and G. Shirane, Z. Phys. B **96**, 465 (1995).

⁶¹ R. J. Birgeneau, M. Greven, M. A. Kastner, Y. S. Lee, B. O. Wells, Y. Endoh, K. Yamada, and G. Shirane, Phys. Rev. B **59**, 13788 (1999).

⁶² I. W. Sumarlin, J. W. Lynn, T. Chatopadhyay, S. N. Barilo, D. I. Zhigunov, and J. L. Peng, Phys. Rev. B **51**, 5824 (1995).

⁶³ A. W. Sandvik, Phys. Rev. B **56**, 11678 (1997).

⁶⁴ N. Schultka and E. Manousakis, Phys. Rev. B **49**, 12071 (1994).

⁶⁵ E. Brezin and J. Zinn-Justin, Phys. Rev. B **14**, 3110 (1976); S. Caracciolo and A. Pelissetto, Nucl. Phys. B **420**, 141 (1994).

⁶⁶ V. Yu. Irkhin and A. A. Katanin, Phys. Lett. A **232**, 143 (1997).